

Auxiliary field diffusion Monte Carlo calculations of light and medium-mass nuclei with local chiral interactions

D. Lonardoni,^{1,2} S. Gandolfi,² J. E. Lynn,^{3,4} C. Petrie,⁵ J. Carlson,² K. E. Schmidt,⁵ and A. Schwenk^{3,4,6}

¹*Facility for Rare Isotope Beams, Michigan State University, East Lansing, Michigan 48824, USA*

²*Theoretical Division, Los Alamos National Laboratory, Los Alamos, New Mexico 87545, USA*

³*Institut für Kernphysik, Technische Universität Darmstadt, 64289 Darmstadt, Germany*

⁴*ExtreMe Matter Institute EMMI, GSI Helmholtzzentrum für Schwerionenforschung GmbH, 64291 Darmstadt, Germany*

⁵*Department of Physics, Arizona State University, Tempe, Arizona 85287, USA*

⁶*Max-Planck-Institut für Kernphysik, Saupfercheckweg 1, 69117 Heidelberg, Germany*



(Received 27 February 2018; published 24 April 2018)

Quantum Monte Carlo methods have recently been employed to study properties of nuclei and infinite matter using local chiral effective-field-theory interactions. In this work, we present a detailed description of the auxiliary field diffusion Monte Carlo algorithm for nuclei in combination with local chiral two- and three-nucleon interactions up to next-to-next-to-leading order. We show results for the binding energy, charge radius, charge form factor, and Coulomb sum rule in nuclei with $3 \leq A \leq 16$. Particular attention is devoted to the effect of different operator structures in the three-body force for different cutoffs. The outcomes suggest that local chiral interactions fit to few-body observables give a very good description of the ground-state properties of nuclei up to ^{16}O , with the exception of one fit for the softer cutoff which predicts overbinding in larger nuclei.

DOI: [10.1103/PhysRevC.97.044318](https://doi.org/10.1103/PhysRevC.97.044318)

I. INTRODUCTION

The solution of the many-body Schrödinger equation describing a system of interacting baryons is challenging because of the nonperturbative nature and the strong spin/isospin dependence of realistic nuclear interactions. Quantum Monte Carlo (QMC) methods provide a powerful tool to tackle the nuclear many-body problem in a nonperturbative fashion. They have been proven to be remarkably successful in describing the properties of strongly correlated fermions in a large variety of physical conditions [1].

Historically, QMC methods have made use of phenomenological nuclear interactions, such as the Argonne v_{18} (AV18) nucleon-nucleon (NN) potential combined with Urbana/Illinois models for the three-nucleon ($3N$) forces [1]. By construction, these potentials are nearly local, meaning that the dominant parts of the interaction depend only on the relative distance, spin, and isospin of the two interacting nucleons, and not upon their momenta. This feature has been one of the keys to success for the application of QMC algorithms to the study of nuclear systems. Green's function Monte Carlo (GFMC) and auxiliary field diffusion Monte Carlo (AFDMC) methods have employed these phenomenological potentials to accurately calculate properties of nuclei, neutron drops, and neutron-star matter [1–8]. Despite the large success of such models, phenomenological interactions are not free from drawbacks. They do not provide a systematic way to estimate theoretical uncertainties, and it is not clear how to improve their quality. In addition, some models of the $3N$ force provide a too soft equation of state of neutron matter [4,9], with the consequence that the predicted neutron-star maximum mass

is not compatible with the observation of heavy neutron stars [10,11].

An alternative approach to nuclear interactions that overcomes the limitations of the phenomenological models is provided by chiral effective field theory (EFT) [12,13]. In chiral EFT, nuclear interactions are systematically derived in connection with the underlying theory of the strong interaction, by writing down the most general Lagrangian consistent with the symmetries of low-energy quantum chromodynamics (QCD) in terms of the relevant degrees of freedom at low energies: nucleons and pions. A power-counting scheme is then chosen to order the resulting contributions according to their importance. The result is a low-energy EFT according to which nuclear forces are given in an expansion in the ratio of a soft scale (the pion mass or a typical momentum scale in the nucleus) to a hard scale (the chiral breakdown scale). The long-range part of the potential is given by pion-exchange contributions that are determined by the chiral symmetry of QCD and low-energy experimental data for the pion-nucleon system. The short-range terms are instead characterized by contact interactions described by so-called low-energy constants (LECs), which are fit to reproduce experimental data (NN scattering data for the two-body part of the interaction, and few- and/or many-body observables for the many-body components). Among the advantages of such an expansion, compared to traditional approaches, are the ability to systematically improve the quality of the interaction order by order, the possibility to estimate theoretical uncertainties, the fact that many-body forces arise naturally, and that electroweak currents can be derived consistently.

In the last decade, intense efforts have been devoted to the development of chiral EFT interactions, as shown by the availability of different potentials in the literature [12–19], typically written in momentum space. It is only in recent years that chiral EFT interactions have been formulated equivalently in coordinate space. New potentials are now available, including next-to-next-to-leading-order (N²LO) local interactions [20,21], supplemented by consistent $3N$ potentials [22,23], as well as chiral interactions with explicit delta degrees of freedom [24–26].

Local chiral interactions up to N²LO can be written using the same operator structure as the phenomenological potentials, providing for the first time the opportunity to combine EFT-derived interactions and accurate QMC methods. The GFMC method has been used to study the ground state of light nuclei employing local chiral interactions [20–23,25–29]. The same potentials have been used in AFDMC calculations of pure neutron systems, ranging from few-body systems [30–32] to pure neutron matter [20–22]. More recently, the first AFDMC study of p -shell nuclei employing local chiral interactions was reported [33]. In this work, we provide a comprehensive description of the AFDMC algorithm for the study of ground-state properties of light and medium-mass nuclei employing local chiral interactions at N²LO, extending the findings of Ref. [33].

The structure of this paper is as follows. In Sec. II we introduce the nuclear Hamiltonian employed in this work. In Secs. III and IV we review the main features of the employed QMC methods. Section V is devoted to the description of the employed trial wave functions. In Sec. VI we present our results for nuclei with $3 \leq A \leq 16$. Finally, we give a summary in Sec. VII.

II. HAMILTONIAN

Nuclei are described as a collection of point-like particles of mass m_N interacting via two- and three-body potentials according to the nonrelativistic Hamiltonian

$$H = -\frac{\hbar^2}{2m_N} \sum_i \nabla_i^2 + \sum_{i<j} v_{ij} + \sum_{i<j<k} V_{ijk}, \quad (1)$$

where the two-body interaction v_{ij} also includes the Coulomb force.

In QMC calculations, it is convenient to express the interactions in terms of radial functions multiplying spin and isospin operators. The commonly employed Argonne v'_8 (AV8') potential [34], as well as the two-body part of the recently developed local chiral interactions [20], can be expressed as

$$v_{ij} = \sum_{p=1}^8 v_p(r_{ij}) \mathcal{O}_{ij}^p, \quad (2)$$

with

$$\mathcal{O}_{ij}^{p=1,8} = [\mathbb{1}, \boldsymbol{\sigma}_i \cdot \boldsymbol{\sigma}_j, S_{ij}, \mathbf{L} \cdot \mathbf{S}] \otimes [\mathbb{1}, \boldsymbol{\tau}_i \cdot \boldsymbol{\tau}_j], \quad (3)$$

where

$$S_{ij} = 3 \boldsymbol{\sigma}_i \cdot \hat{\mathbf{r}}_{ij} \boldsymbol{\sigma}_j \cdot \hat{\mathbf{r}}_{ij} - \boldsymbol{\sigma}_i \cdot \boldsymbol{\sigma}_j \quad (4)$$

is the tensor operator, and

$$\mathbf{L} = \frac{1}{2i} (\mathbf{r}_i - \mathbf{r}_j) \times (\nabla_i - \nabla_j), \quad (5)$$

$$\mathbf{S} = \frac{1}{2} (\boldsymbol{\sigma}_i + \boldsymbol{\sigma}_j) \quad (6)$$

are the relative angular momentum and the total spin of the pair ij , respectively. The radial functions of Eq. (2) are fitted to NN scattering data. At N²LO, the operator structure of the local chiral interactions is the same as above, with the only exception that the $\mathbf{L} \cdot \mathbf{S} \boldsymbol{\tau}_i \cdot \boldsymbol{\tau}_j$ term is not present at N²LO. In this work, we consider LO, NLO, and N²LO two-body potentials of Ref. [21] with spectral-function cutoff $\tilde{\Lambda} = 1000$ MeV and coordinate-space cutoffs $R_0 = 1.0$ fm and $R_0 = 1.2$ fm, approximately corresponding to cutoffs in momentum space of 500 and 400 MeV [28] (note, however, also Ref. [35]).

The three-body force V_{ijk} is written as a sum of contributions coming from two-pion exchange (TPE), plus shorter-range terms. In the case of local chiral interactions at N²LO, P - and S -wave TPE contributions are included, and they are characterized by the same LECs involved in the two-body sector. The shorter-range part of the $3N$ force is instead parametrized by two contact terms, the LECs of which have been fit to the α -particle binding energy and to the spin-orbit splitting in the neutron- α P -wave phase shifts (see Refs. [23,28] for more details).

The chiral $3N$ interaction at N²LO can be conveniently written as

$$V = V_a^{2\pi,P} + V_c^{2\pi,P} + V^{2\pi,S} + V_D + V_E, \quad (7)$$

where the first three terms correspond to the TPE diagrams in P and S waves (Eqs. (A1b), (A1c), and (A1a) of Ref. [28], respectively). The subscripts a and c refer to the operator structure of such contributions, which can be written in terms of anticommutators or commutators, respectively. V_D and V_E involve contact terms. In this work, we employ the form (A2b) of Ref. [28] for V_D , and we consider two choices for V_E , namely $E\tau$ and $E\mathbb{1}$ (Eqs. (A3a) and (A3b) of Ref. [28]).

By defining the quantities

$$\begin{aligned} \delta_{R_0}(r) &= \frac{n}{4\pi R_0^3 \Gamma(3/n)} e^{-(r/R_0)^n}, \\ T(r) &= \left(1 + \frac{3}{m_\pi r} + \frac{3}{m_\pi^2 r^2}\right) \frac{e^{-m_\pi r}}{m_\pi r} T_c(r), \\ Y(r) &= \frac{e^{-m_\pi r}}{m_\pi r} Y_c(r), \\ Z(r) &= \frac{m_\pi r}{3} (Y(r) - T(r)), \\ Y_c(r) &= 1 - e^{-(r/R_0)^n}, \\ T_c(r) &= (1 - e^{-(r/R_0)^n})^{n_1}, \\ X_{i\alpha j\beta} &= (3 \delta_{\alpha\gamma} \hat{r}_{ij}^\gamma \delta_{\beta\mu} \hat{r}_{ij}^\mu - \delta_{\alpha\beta}) T(r_{ij}) + \delta_{\alpha\beta} Y(r_{ij}), \\ \mathcal{X}_{i\alpha j\beta} &= X_{i\alpha j\beta}(\mathbf{r}_{ij}) - \delta_{\alpha\beta} \frac{4\pi}{m_\pi^3} \delta_{R_0}(r_{ij}), \\ \mathcal{Z}_{ij\alpha} &= Z(r_{ij}) \delta_{\alpha\gamma} \hat{r}_{ij}^\gamma, \end{aligned} \quad (8)$$

we can recast the contributions of Eq. (7) in a form that is suitable for QMC calculations:

$$\begin{aligned}
 V_a^{2\pi,P} &= A_a^{2\pi,P} \sum_{i<j<k} \sum_{\text{cyc}} \{\boldsymbol{\tau}_i \cdot \boldsymbol{\tau}_k, \boldsymbol{\tau}_j \cdot \boldsymbol{\tau}_k\} \{\sigma_i^\alpha \sigma_k^\gamma, \sigma_k^\mu \sigma_j^\beta\} \mathcal{X}_{i\alpha k\gamma} \mathcal{X}_{k\mu j\beta} \\
 &= 4 A_a^{2\pi,P} \sum_{i<j} \boldsymbol{\tau}_i \cdot \boldsymbol{\tau}_j \sigma_i^\alpha \sigma_j^\beta \sum_{k \neq i,j} \mathcal{X}_{i\alpha k\gamma} \mathcal{X}_{k\mu j\beta} \\
 &= 4 A_a^{2\pi,P} \sum_{i<j} \boldsymbol{\tau}_i \cdot \boldsymbol{\tau}_j \sigma_i^\alpha \sigma_j^\beta \sum_{k \neq i,j} \left(X_{i\alpha k\gamma} - \delta_{\alpha\gamma} \frac{4\pi}{m_\pi^3} \delta_{R_0}(r_{ik}) \right) \left(X_{k\mu j\beta} - \delta_{\mu\beta} \frac{4\pi}{m_\pi^3} \delta_{R_0}(r_{kj}) \right) \\
 &= V_a^{XX} + V_a^{X\delta} + V_a^{\delta\delta}, \tag{9}
 \end{aligned}$$

$$\begin{aligned}
 V_c^{2\pi,P} &= A_c^{2\pi,P} \sum_{i<j<k} \sum_{\text{cyc}} [\boldsymbol{\tau}_i \cdot \boldsymbol{\tau}_k, \boldsymbol{\tau}_j \cdot \boldsymbol{\tau}_k] [\sigma_i^\alpha \sigma_k^\gamma, \sigma_k^\mu \sigma_j^\beta] \mathcal{X}_{i\alpha k\gamma} \mathcal{X}_{k\mu j\beta} \\
 &= A_c^{2\pi,P} \sum_{i<j<k} \sum_{\text{cyc}} [\boldsymbol{\tau}_i \cdot \boldsymbol{\tau}_k, \boldsymbol{\tau}_j \cdot \boldsymbol{\tau}_k] [\sigma_i^\alpha \sigma_k^\gamma, \sigma_k^\mu \sigma_j^\beta] \left(X_{i\alpha k\gamma} - \delta_{\alpha\gamma} \frac{4\pi}{m_\pi^3} \delta_{R_0}(r_{ik}) \right) \left(X_{k\mu j\beta} - \delta_{\mu\beta} \frac{4\pi}{m_\pi^3} \delta_{R_0}(r_{kj}) \right) \\
 &= V_c^{XX} + V_c^{X\delta} + V_c^{\delta\delta}, \tag{10}
 \end{aligned}$$

$$\begin{aligned}
 V^{2\pi,S} &= A^{2\pi,S} \sum_{i<j<k} \sum_{\text{cyc}} \boldsymbol{\tau}_i \cdot \boldsymbol{\tau}_j \sigma_i^\alpha \sigma_j^\beta \mathcal{Z}_{i\alpha k} \mathcal{Z}_{j\beta k\alpha} \\
 &= A^{2\pi,S} \sum_{i<j} \boldsymbol{\tau}_i \cdot \boldsymbol{\tau}_j \sigma_i^\alpha \sigma_j^\beta \sum_{k \neq i,j} \mathcal{Z}_{i\alpha k} \mathcal{Z}_{j\beta k\alpha}, \tag{11}
 \end{aligned}$$

$$\begin{aligned}
 V_D &= A_D \sum_{i<j} \boldsymbol{\tau}_i \cdot \boldsymbol{\tau}_j \sigma_i^\alpha \sigma_j^\beta \sum_{k \neq i,j} \mathcal{X}_{i\alpha j\beta} [\delta_{R_0}(r_{ik}) + \delta_{R_0}(r_{jk})] \\
 &= A_D \sum_{i<j} \boldsymbol{\tau}_i \cdot \boldsymbol{\tau}_j \sigma_i^\alpha \sigma_j^\beta \sum_{k \neq i,j} \left(X_{i\alpha j\beta} - \delta_{\alpha\beta} \frac{4\pi}{m_\pi^3} \delta_{R_0}(r_{ij}) \right) [\delta_{R_0}(r_{ik}) + \delta_{R_0}(r_{jk})] \\
 &= V_D^{X\delta} + V_D^{\delta\delta}, \tag{12}
 \end{aligned}$$

$$V_E = A_E \sum_{i<j} \boldsymbol{\tau}_i \cdot \boldsymbol{\tau}_j \sum_{k \neq i,j} \delta_{R_0}(r_{ik}) \delta_{R_0}(r_{jk}), \tag{13}$$

where the sum over the coordinate projections (greek indices) is implicit. Equation (13) is the expression for the $E\tau$ parametrization of the contact term V_E . The $E\mathbb{1}$ form is recovered by setting $\boldsymbol{\tau}_i \cdot \boldsymbol{\tau}_j = \mathbb{1}$. For the local chiral interactions at $N^2\text{LO}$, we have

$$\begin{aligned}
 A_a^{2\pi,P} &= \frac{1}{2} \left(\frac{g_A}{f_\pi^2} \right)^2 \left(\frac{1}{4\pi} \right)^2 \frac{m_\pi^6}{9} c_3, \\
 A_c^{2\pi,P} &= -\frac{c_4}{2c_3} A_a^{2\pi,P}, \\
 A^{2\pi,S} &= \left(\frac{g_A}{2f_\pi} \right)^2 \left(\frac{m_\pi}{4\pi} \right)^2 \frac{4m_\pi^6}{f_\pi^2} c_1, \tag{14} \\
 A_D &= \frac{m_\pi^3}{12\pi} \frac{g_A}{8f_\pi^2} \frac{1}{f_\pi^2 \Lambda_\chi} c_D, \\
 A_E &= \frac{c_E}{f_\pi^4 \Lambda_\chi},
 \end{aligned}$$

where $g_A = 1.267$ is the axial-vector coupling constant, $f_\pi = 92.4$ MeV is the pion decay constant, $m_\pi = 138.03$ MeV is the averaged pion mass, Λ_χ is taken to be a heavy meson scale $\Lambda_\chi = 700$ MeV, and c_1, c_3, c_4, c_D, c_E are the LECs. Note that,

using these definitions, the structure of the phenomenological Urbana IX (UIX) model is recovered by imposing $\delta_{R_0}(r) = 0$, $n = 2, n_t = 2$, and $A_c^{2\pi,P} = \frac{1}{4} A_a^{2\pi,P}$ as well as $A_D = A_E = 0$.

III. REVIEW OF THE VMC METHOD

In the variational Monte Carlo (VMC) method, given a trial wave function Ψ_T , the expectation value of the Hamiltonian H is given by

$$E_0 \leq \langle H \rangle = \frac{\langle \Psi_T | H | \Psi_T \rangle}{\langle \Psi_T | \Psi_T \rangle} = \frac{\int dR \Psi_T^*(R) H \Psi_T(R)}{\int dR \Psi_T^*(R) \Psi_T(R)}, \tag{15}$$

where $R = \{\mathbf{r}_1, \dots, \mathbf{r}_A\}$ are the coordinates of the particles, and there is an implicit sum over all the particle spin and isospin states. E_0 is the energy of the true ground state with the same quantum numbers as Ψ_T , and the leftmost equality in the above relation is valid only if the wave function is the exact ground-state wave function Ψ_0 . In the VMC method, one typically minimizes the energy expectation value of Eq. (15) with respect to changes in the variational parameters, in order to obtain Ψ_T as close as possible to Ψ_0 .

The integral of Eq. (15) can be rewritten as

$$\langle H \rangle = \frac{\int dR P(R) \frac{H\Psi_T(R)}{\Psi_T(R)}}{\int dR P(R)}, \quad (16)$$

where $P(R) = |\Psi_T(R)|^2$ can be interpreted as a probability distribution of points R in a $3A$ -dimensional space. The above multidimensional integral can be solved using Monte Carlo sampling. In practice, a number of configurations R_i are sampled using the Metropolis algorithm [36], and the local energy of the system is calculated as

$$\langle E \rangle = \frac{1}{A} \sum_{i=1}^A \frac{\langle R_i | H | \Psi_T \rangle}{\langle R_i | \Psi_T \rangle}, \quad (17)$$

where $\langle R | \Psi_T \rangle = \Psi_T(R)$. More details on the sampling procedure and on the calculation of statistical errors can be found, e.g., in Ref. [37].

For spin/isospin-dependent interactions the generalization of Eq. (15) is straightforward:

$$\langle H \rangle = \frac{\int dR \sum_{S,S'} \Psi_T^*(R,S') H_{S,S'} \Psi_T(R,S)}{\int dR \sum_S |\Psi_T(R,S)|^2}, \quad (18)$$

where now the wave function also depends upon spin and isospin states $S = \{s_1, \dots, s_A\}$, and

$$H_{S,S'} = \langle S' | S \rangle \left[-\frac{\hbar^2}{2m} \sum_i \nabla_i^2 \right] + \langle RS' | V | RS \rangle. \quad (19)$$

In this case, the VMC method can be implemented by either explicitly summing over all the spin and isospin states,

$$\begin{aligned} \langle H \rangle &= \int dR E_L(R) P(R), \\ P(R) &= \frac{\sum_S |\Psi_T(R,S)|^2}{\int dR \sum_S |\Psi_T(R,S)|^2}, \\ E_L(R) &= \frac{\sum_{S,S'} \Psi_T^*(R,S') H_{S,S'} \Psi_T(R,S)}{\sum_S |\Psi_T(R,S)|^2}, \end{aligned} \quad (20)$$

or by sampling the spin and isospin states

$$\begin{aligned} \langle H \rangle &= \int dR \sum_S E_L(R,S) P(R,S), \\ P(R,S) &= \frac{|\Psi_T(R,S)|^2}{\int dR |\Psi_T(R,S)|^2}, \\ E_L(R,S) &= \frac{\sum_{S'} \Psi_T^*(R,S') H_{S,S'} \Psi_T(R,S)}{|\Psi_T(R,S)|^2}. \end{aligned} \quad (21)$$

The Metropolis algorithm can then be used to sample either R from $P(R)$ in the former case, or R and S from $P(R,S)$ in the latter case.

IV. REVIEW OF THE AFDMC METHOD

Diffusion Monte Carlo (DMC) methods are used to project out the ground state with a particular set of quantum numbers. The starting point is a trial wave function $|\Psi_T\rangle$, typically the result of a VMC minimization, that is propagated in imaginary

time τ :

$$|\Psi_0\rangle \propto \lim_{\tau \rightarrow \infty} e^{-(H-E_T)\tau} |\Psi_T\rangle, \quad (22)$$

where E_T is a parameter that controls the normalization. For spin/isospin-independent interactions, the object to be propagated is given by the overlap between the wave function and a set of configurations in coordinate space $\langle R | \Psi_T \rangle = \Psi_T(R)$. By using the completeness relation $\int dR |R\rangle \langle R| = \mathbb{1}$, we can write the propagation in imaginary time as

$$\langle R' | \Psi(\tau) \rangle = \int dR G(R', R, \tau) \langle R | \Psi_T(0) \rangle, \quad (23)$$

where the propagator (or Green's function) G is defined as the matrix element between the two points R and R' in the volume

$$G(R', R, \tau) = \langle R' | e^{-(H-E_T)\tau} | R \rangle, \quad (24)$$

and $\langle R' | \Psi(\tau) \rangle$ approaches the true ground state for large imaginary time.

In practice, it is not possible to directly compute the propagator $G(R', R, \tau)$. However, one can use the short-time propagator $G(R', R, d\tau)$,

$$\begin{aligned} \langle R' | \Psi(\tau) \rangle &= \int dR_n dR_{n-1} \dots dR_1 dR G(R', R_n, \delta\tau) \\ &\times G(R_{n-1}, R_{n-2}, \delta\tau) \dots G(R_1, R, \delta\tau) \langle R | \Psi_T(0) \rangle, \end{aligned} \quad (25)$$

and then employ Monte Carlo techniques to sample the paths R_i in the imaginary-time evolution. The method is accurate for small values of the time step $\delta\tau$, and the exact result can be determined by using different values of $\delta\tau$ and extrapolating to $\delta\tau \rightarrow 0$.

By using the Trotter formula [38] to order $d\tau^3$, the short-time propagator can be approximated with

$$\begin{aligned} G(R', R, \delta\tau) &\equiv \langle R' | e^{-(H-E_T)\delta\tau} | R \rangle \\ &\approx \langle R' | e^{-(V-E_T)\frac{\delta\tau}{2}} e^{-T\delta\tau} e^{-(V-E_T)\frac{\delta\tau}{2}} | R \rangle, \end{aligned} \quad (26)$$

where T is the nonrelativistic kinetic energy, and V is the employed potential. The propagator for the kinetic energy alone corresponds to the free-particle propagator

$$\begin{aligned} G_0(R', R) &= \langle R' | e^{-T\delta\tau} | R \rangle \\ &= \left(\frac{m}{2\pi\hbar^2\delta\tau} \right)^{\frac{3A}{2}} e^{-\frac{m(R-R')^2}{2\hbar^2\delta\tau}}, \end{aligned} \quad (27)$$

which yields a Gaussian diffusion for the paths in coordinate space, with $\sigma^2 = 4\frac{\hbar^2}{2m}\delta\tau$. The propagator for spin/isospin-independent potentials is simply given by

$$\langle R' | e^{-(V-E_T)\delta\tau} | R \rangle \approx \prod_{i<j} e^{-[V(r_{ij})-E_T]\delta\tau} \delta(R-R'), \quad (28)$$

where each pair interaction can be simply evaluated as a function of the coordinates of the system, and the energy E_T results in a normalization factor. Note that the addition of spin/isospin-independent three- and many-body interactions is straightforward.

For spin/isospin-dependent interactions, the propagation of the potential becomes more complicated. In general, this is

because quadratic operators like $\sigma_i \cdot \sigma_j$ generate amplitudes along the singlet and the triplet states of a pair. The propagator of Eq. (28) generalizes in this case to

$$\begin{aligned} \langle R' | e^{-(V-E_T)\delta\tau} | R \rangle &\rightarrow \langle R' S' | e^{-(V-E_T)\delta\tau} | R S \rangle \\ &\approx \langle S' | \prod_{i<j} e^{-(V(r_{ij})-E_T)\delta\tau} | S \rangle \delta(R - R'), \end{aligned} \quad (29)$$

where now the matrix $\exp[-(V - E_T)\delta\tau]$ is not diagonal in the spin of each pair. One possible strategy to compute the propagator of Eq. (29) is to include all the spin and isospin states in the trial wave function, as is done in GFMC calculations [1]. This, however, implies a number of wave-function components proportional to 2^A , which currently limits GFMC calculations to $A = 12$.

The idea of the AFDMC method is to start from a trial wave function whose computational cost is polynomial with A , rather than exponential. Such a wave function can be written in the single-particle representation

$$\langle S | \Psi \rangle \propto \xi_{\alpha_1}(s_1) \xi_{\alpha_2}(s_2) \cdots \xi_{\alpha_A}(s_A), \quad (30)$$

where $\xi_{\alpha_i}(s_i)$ are functions of the spinor s_i with state α_i . In the above expression, the radial orbitals are omitted for simplicity, and the antisymmetrization is trivial.

A quadratic operator in the spin acting on the wave function above generates two different amplitudes,

$$\begin{aligned} \langle S | \sigma_1 \cdot \sigma_2 | \Psi \rangle &= \langle S | 2\mathcal{P}_{12}^\sigma - \mathbb{1} | \Psi \rangle \\ &= 2 \xi_{\alpha_1}(s_2) \xi_{\alpha_2}(s_1) \xi_{\alpha_3}(s_3) \cdots \xi_{\alpha_A}(s_A) \\ &\quad - \xi_{\alpha_1}(s_1) \xi_{\alpha_2}(s_2) \xi_{\alpha_3}(s_3) \cdots \xi_{\alpha_A}(s_A) \\ &= \langle S' | \Psi \rangle + \langle S'' | \Psi \rangle. \end{aligned} \quad (31)$$

In general, the action of all pairwise spin/isospin operators (or propagators) generates $2^A \binom{A}{Z}$ amplitudes (if charge

conservation is imposed). Even though this number can be further reduced by assuming that the nucleus has good isospin [1], the action of pairwise operators largely increases the number of components with respect to the initial wave function, thus losing the computational advantage of the polynomial scaling with A . However, linear spin/isospin operators do not break the single-particle representation. They simply imply rotations of the initial spinors, without generating new amplitudes, as for instance

$$\begin{aligned} \langle S | \sigma_1^\alpha | \Psi \rangle &= \sigma_1^\alpha \xi_{\alpha_1}(s_1) \xi_{\alpha_2}(s_2) \xi_{\alpha_3}(s_3) \cdots \xi_{\alpha_A}(s_A) \\ &= \xi_{\alpha_1}(s'_1) \xi_{\alpha_2}(s_2) \xi_{\alpha_3}(s_3) \cdots \xi_{\alpha_A}(s_A) \\ &= \langle S' | \Psi \rangle. \end{aligned} \quad (32)$$

Quadratic operators can be linearized by using the Hubbard-Stratonovich transformation

$$e^{-\frac{1}{2}\lambda\mathcal{O}^2} = \frac{1}{\sqrt{2\pi}} \int dx e^{-\frac{x^2}{2} + \sqrt{-\lambda}x\mathcal{O}}, \quad (33)$$

where x are usually called auxiliary fields, and the integral above can be computed with Monte Carlo techniques, i.e., by sampling points x with probability distribution $P(x) = \exp(-x^2/2)$. By using the transformation of Eq. (33), Hamiltonians involving up to quadratic operators in spin and isospin can be efficiently employed in the imaginary-time propagation of a trial wave function of the form of Eq. (30), retaining the good polynomial scaling with A .

A. Propagation of spin/isospin quadratic operators

Let us consider the two-body interaction of Eq. (2) up to $p = 6$,

$$\begin{aligned} V_{NN}^6 &= \sum_{i<j} \{ [v_1(r_{ij}) + v_2(r_{ij}) \boldsymbol{\tau}_i \cdot \boldsymbol{\tau}_j] \mathbb{1} + [v_3(r_{ij}) + v_4(r_{ij}) \boldsymbol{\tau}_i \cdot \boldsymbol{\tau}_j] \sigma_i \cdot \sigma_j + [v_5(r_{ij}) + v_6(r_{ij}) \boldsymbol{\tau}_i \cdot \boldsymbol{\tau}_j] S_{ij} \} \\ &= \sum_{i<j} v_1(r_{ij}) + \sum_{i<j} [v_2(r_{ij})] \boldsymbol{\tau}_i \cdot \boldsymbol{\tau}_j + \sum_{i<j} \sum_{\alpha\beta} [v_3(r_{ij}) \delta_{\alpha\beta} + v_5(r_{ij}) (3 \hat{r}_{ij}^\alpha \hat{r}_{ij}^\beta - \delta_{\alpha\beta})] \sigma_i^\alpha \sigma_j^\beta \\ &\quad + \sum_{i<j} \sum_{\alpha\beta} [v_4(r_{ij}) \delta_{\alpha\beta} + v_6(r_{ij}) (3 \hat{r}_{ij}^\alpha \hat{r}_{ij}^\beta - \delta_{\alpha\beta})] \boldsymbol{\tau}_i \cdot \boldsymbol{\tau}_j \sigma_i^\alpha \sigma_j^\beta \\ &= V_{SI}(R) + \frac{1}{2} \sum_{i \neq j} A_{ij}^{(\tau)} \boldsymbol{\tau}_i \cdot \boldsymbol{\tau}_j + \frac{1}{2} \sum_{i \neq j} \sum_{\alpha\beta} A_{i\alpha j\beta}^{(\sigma)} \sigma_i^\alpha \sigma_j^\beta + \frac{1}{2} \sum_{i \neq j} \sum_{\alpha\beta} A_{i\alpha j\beta}^{(\sigma\tau)} \boldsymbol{\tau}_i \cdot \boldsymbol{\tau}_j \sigma_i^\alpha \sigma_j^\beta \\ &= V_{SI}(R) + V_{SD}(R), \end{aligned} \quad (34)$$

where V_{SI} (V_{SD}) is the spin/isospin-independent (-dependent) part of the interaction, and $A_{ij}^{(\tau)}$ ($A \times A$), $A_{i\alpha j\beta}^{(\sigma)}$ ($3A \times 3A$), and $A_{i\alpha j\beta}^{(\sigma\tau)}$ ($3A \times 3A$) are real and symmetric matrices. As such, these matrices can be diagonalized,

$$\begin{aligned} \sum_j A_{ij}^{(\tau)} \psi_{n,j}^{(\tau)} &= \lambda_n^{(\tau)} \psi_{n,i}^{(\tau)}, \\ \sum_{j\beta} A_{i\alpha j\beta}^{(\sigma)} \psi_{n,j\beta}^{(\sigma)} &= \lambda_n^{(\sigma)} \psi_{n,i\alpha}^{(\sigma)}, \\ \sum_{j\beta} A_{i\alpha j\beta}^{(\sigma\tau)} \psi_{n,j\beta}^{(\sigma\tau)} &= \lambda_n^{(\sigma\tau)} \psi_{n,i\alpha}^{(\sigma\tau)}, \end{aligned} \quad (35)$$

and it is possible to define a new set of operators expressed in terms of their eigenvectors,

$$\begin{aligned}\mathcal{O}_{n\alpha}^{(\tau)} &= \sum_j \tau_j^\alpha \psi_{n,j}^{(\tau)}, \\ \mathcal{O}_n^{(\sigma)} &= \sum_{j\beta} \sigma_j^\beta \psi_{n,j\beta}^{(\sigma)}, \\ \mathcal{O}_{n\alpha}^{(\sigma\tau)} &= \sum_{j\beta} \tau_j^\alpha \sigma_j^\beta \psi_{n,j\beta}^{(\sigma\tau)},\end{aligned}\quad (36)$$

such that the spin/isospin-dependent part of Eq. (34) can be recast as

$$\begin{aligned}V_{SD}(R) &= \frac{1}{2} \sum_{\alpha=1}^3 \sum_{n=1}^A \lambda_n^{(\tau)} (\mathcal{O}_{n\alpha}^{(\tau)})^2 + \frac{1}{2} \sum_{n=1}^{3A} \lambda_n^{(\sigma)} (\mathcal{O}_n^{(\sigma)})^2 \\ &+ \frac{1}{2} \sum_{\alpha=1}^3 \sum_{n=1}^{3A} \lambda_n^{(\sigma\tau)} (\mathcal{O}_{n\alpha}^{(\sigma\tau)})^2.\end{aligned}\quad (37)$$

The potential written in this form contains only quadratic operators in spin/isospin. We can thus use the Hubbard-Stratonovich transformation of Eq. (33) to write the propagator of the V_{NN}^6 interaction acting on a configuration $|RS\rangle$ as

$$\begin{aligned}e^{-V_{NN}^6 \delta\tau} |RS\rangle &= e^{-V_{SI}(R)\delta\tau} \prod_{m=1}^{15A} \frac{1}{\sqrt{2\pi}} \\ &\times \int dx_m e^{\frac{\gamma_m}{2}} e^{\sqrt{-\lambda_m \delta\tau} x_m} \mathcal{O}_m |RS\rangle = |RS'\rangle,\end{aligned}\quad (38)$$

where 15 auxiliary fields are needed for each nucleon: 3 for τ operators, 3 for σ , and 9 for $\sigma\tau$. The propagation (rotation) of spinors depends upon the sampling of the auxiliary fields $X = \{x_m\}$; so does the new spin/isospin configurations $S' \equiv S'(X)$. The full short-time propagator, which includes both kinetic and potential energies, can finally be expressed as

$$\begin{aligned}G(R', R, S'(X), S, \delta\tau) &= \langle R' S' | \left(\frac{m}{2\pi \hbar^2 \delta\tau} \right)^{\frac{3A}{2}} e^{-\frac{m(R-R')^2}{2\hbar^2 \delta\tau}} e^{-(V_{SI}(R) - E_T)\delta\tau} \prod_{m=1}^{15A} \frac{1}{\sqrt{2\pi}} \\ &\times \int dx_m e^{-\frac{\gamma_m}{2}} e^{\sqrt{-\lambda_m \delta\tau} x_m} \mathcal{O}_m |RS\rangle.\end{aligned}\quad (39)$$

Note that the above expressions refer to the simple propagator $\exp[-T\delta\tau] \exp[-(V - E_T)\delta\tau]$. In practice, we sample the more accurate propagator $\exp[-(V - E_T)\delta\tau/2] \exp[-T\delta\tau] \exp[-(V - E_T)\delta\tau/2]$, which implies two sets of rotations in $\delta\tau/2$: the first depending on R , and the second on the diffused R' , for a total of 30 auxiliary fields. Compared to the GFMC method, where the coordinates are sampled and the spin and isospin states are explicitly included and summed, in AFDMC, spin and isospin are also sampled via Hubbard-Stratonovich rotations. This largely reduces the computational cost of the imaginary-time propagation of a many-body wave function, allowing one to calculate nuclei more efficiently up ^{12}C , and to go beyond $A = 12$.

B. Propagation of spin-orbit operators

The spin-orbit operator reads

$$v_{LS}(r_{ij}) = v_7(r_{ij}) \mathbf{L} \cdot \mathbf{S}, \quad (40)$$

where \mathbf{L} and \mathbf{S} are defined in Eqs. (5) and (6), respectively. As shown in Ref. [39], one way to evaluate the propagator for spin-orbit operators is to consider the expansion at first order in $\delta\tau$,

$$e^{-v_7(r_{ij}) \mathbf{L} \cdot \mathbf{S} \delta\tau} \approx \mathbb{1} - v_7(r_{ij}) \mathbf{L} \cdot \mathbf{S} \delta\tau, \quad (41)$$

acting on the free propagator G_0 of Eq. (27). The resulting propagator is

$$\begin{aligned}G_{LS} &\approx \exp \left(\sum_{i \neq j} \frac{1}{8i} \frac{2m}{\hbar^2} v_7(r_{ij}) (\mathbf{r}_i - \mathbf{r}_j) \right. \\ &\left. \times (\Delta \mathbf{r}_i - \Delta \mathbf{r}_j) \cdot (\boldsymbol{\sigma}_i + \boldsymbol{\sigma}_j) \right),\end{aligned}\quad (42)$$

where $\Delta \mathbf{r}_i = \mathbf{r}_i - \mathbf{r}'_i$ is the difference of the particle position before and after the action of the free propagator G_0 . Note that the above propagator is only linear in the spin, i.e., it does not require any auxiliary field to be sampled. However, it can be shown that it induces spurious counter terms [9]. These can be removed by using the modified propagator

$$\begin{aligned}G_{LS} &\approx \exp \left(\sum_{i \neq j} \frac{1}{4i} \frac{m}{\hbar^2 \delta\tau} v_7(r_{ij}) [\mathbf{r}_{ij} \times \Delta \mathbf{r}_{ij}] \cdot \boldsymbol{\sigma}_i \right) \\ &\times \exp \left(-\frac{1}{2} \left[\sum_{i \neq j} \frac{1}{4i} \frac{m}{\hbar^2} v_7(r_{ij}) [\mathbf{r}_{ij} \times \Delta \mathbf{r}_{ij}] \cdot \boldsymbol{\sigma}_i \right]^2 \right).\end{aligned}\quad (43)$$

This alternative version of the spin-orbit propagator contains quadratic spin operators, and thus it requires additional Hubbard-Stratonovich fields to be sampled, but it is correct at order $\delta\tau$.

C. Propagation of three-body forces

Several terms of the $3N$ interaction [Eq. (7)] can be directly included in the AFDMC propagator. These are $V_a^{2\pi, P}$, $V^{2\pi, S}$, V_D , and V_E of Eqs. (9) and (11)–(13), which correspond to terms involving only quadratic spin and isospin operators. These have the same operator structure as the spin/isospin-dependent part of the two-body potential (Eq. (34)). The dependence on the third particle k enters only in the radial functions $\mathcal{X}_{i\alpha j\beta}$, $\mathcal{Z}_{ij\alpha}$, and $\delta_{R_0}(r)$, which can be absorbed in the definition of the matrices $A_{ij}^{(\tau)}$ and $A_{i\alpha j\beta}^{(\sigma\tau)}$.

The structure of $V_c^{2\pi, P}$ contains instead cubic spin and isospin operators, and the Hubbard-Stratonovich transformation of Eq. (33) cannot be applied. It follows that these terms cannot be exactly included in the standard AFDMC propagation. It may be possible to invoke more complicated algorithms to sample them, but the imaginary-time step will need to be higher order in $\delta\tau$. However, their expectation

value can always be calculated, and it can be used to derive an approximate three-body propagator for $V_c^{2\pi,P}$.

Let us define an effective Hamiltonian H' that can be exactly included in the AFDMC propagation:

$$H' = H - V_c^{2\pi,P} + \alpha_1 V_a^{XX} + \alpha_2 V_D^{X\delta} + \alpha_3 V_E. \quad (44)$$

The three constants α_i are adjusted in order to have

$$\begin{aligned} \langle V_c^{XX} \rangle &\approx \langle \alpha_1 V_a^{XX} \rangle, \\ \langle V_c^{X\delta} \rangle &\approx \langle \alpha_2 V_D^{X\delta} \rangle, \\ \langle V_c^{\delta\delta} \rangle &\approx \langle \alpha_3 V_E \rangle, \end{aligned} \quad (45)$$

where $\langle \dots \rangle$ indicates the average over the wave function (see Sec. IV E), and the identifications are suggested by the similar ranges and functional forms.

Once the ground state Ψ'_0 of H' is calculated via the AFDMC imaginary-time propagation, the expectation value of the Hamiltonian H is given by

$$\begin{aligned} \langle H \rangle &\approx \langle \Psi'_0 | H' | \Psi'_0 \rangle + \langle \Psi'_0 | H - H' | \Psi'_0 \rangle \\ &\approx \langle H' \rangle + \langle V_c^{2\pi,P} - \alpha_1 V_a^{XX} - \alpha_2 V_D^{X\delta} - \alpha_3 V_E \rangle \\ &\approx \langle H' \rangle + \langle V_{\text{pert}} \rangle, \end{aligned} \quad (46)$$

where the last term is evaluated perturbatively, meaning that its expectation value is calculated, even though not all the operators are included in the propagator ($V_c^{2\pi,P}$). By opportunely adjusting the constants α_i of Eq. (45), we ensure that the correction $\langle V_{\text{pert}} \rangle$ is small compared to $\langle H' \rangle$. A similar approach is used in the GFMC method to calculate the small nonlocal terms that are present in the AV18 interaction. In that case the difference $v'_8 - v_{18}$ is calculated as a perturbation [40].

D. Importance sampling

Diffusion Monte Carlo algorithms, such as the GFMC and AFDMC methods, are much more efficient when importance sampling techniques are also implemented. In fact, sampling spatial and spin/isospin configurations according to $G(R', R, S', (X), S, \delta\tau)$ might not always be efficient. For instance, consider the case of a strongly repulsive interaction at short distances. In such a situation, sampling the spatial coordinates according to the kinetic energy only is not an optimal choice because no information about the interaction is included in sampling the paths, but only through the weights associated with the configurations. As a result, an inefficiently sampled path might have a very small weight, making its contribution very small along the imaginary time.

Suppose that we construct a positive definite wave function Ψ_G close to that of the true ground state of the Hamiltonian H . Ψ_G can be used to guide the imaginary-time evolution by defining a better propagator compared to that of Eq. (23), to be used to sample coordinates and spin/isospin configurations:

$$\begin{aligned} &\langle \Psi_G | R' S' \rangle \langle R' S' | \Psi(\delta\tau) \rangle \\ &= \int dR G(R', R, S'(X), S, \delta\tau) \langle \Psi_G | R' S'(X) \rangle \langle RS | \Psi_T(0) \rangle \end{aligned}$$

$$\begin{aligned} &= \int dR G(R', R, S'(X), S, \delta\tau) \\ &\quad \times \frac{\langle \Psi_G | R' S'(X) \rangle}{\langle \Psi_G | RS \rangle} \langle \Psi_G | RS \rangle \langle RS | \Psi_T(0) \rangle. \end{aligned} \quad (47)$$

Note that if Ψ_G is positive definite, the above propagation does not change the variance of the computed observables.

In typical DMC calculations the modified propagator is sampled by shifting the Gaussian in the free propagator, and then including the local energy in the weight of the configuration (see, e.g., Ref. [41]). A similar approach has also been used in AFDMC calculations in the past. However, in the latest implementation of the AFDMC method, a much more efficient way to implement the importance sampling propagator is used.

The goal is to sample the modified propagator

$$G(R', R, S'(X), S, \delta\tau) \frac{\langle \Psi_G | R' S'(X) \rangle}{\langle \Psi_G | RS \rangle}. \quad (48)$$

We first sample a set of coordinate displacements ΔR according to Eq. (39) and a set of auxiliary fields X from Gaussian distributions. Since the propagator G implies the Gaussian sampling for the kinetic energy and for the auxiliary fields, sampling ΔR and X has the same probability of sampling $-\Delta R$ and $-X$. Driven by this observation, we calculate the ratios

$$\begin{aligned} w_1 &= \frac{\langle \Psi_G | R + \Delta R, S'(X) \rangle}{\langle \Psi_G | RS \rangle} e^{-[V_{SI}(R+\Delta R) - E_T]\delta\tau}, \\ w_2 &= \frac{\langle \Psi_G | R - \Delta R, S'(X) \rangle}{\langle \Psi_G | RS \rangle} e^{-[V_{SI}(R-\Delta R) - E_T]\delta\tau}, \\ w_3 &= \frac{\langle \Psi_G | R + \Delta R, S'(-X) \rangle}{\langle \Psi_G | RS \rangle} e^{-[V_{SI}(R+\Delta R) - E_T]\delta\tau}, \\ w_4 &= \frac{\langle \Psi_G | R - \Delta R, S'(-X) \rangle}{\langle \Psi_G | RS \rangle} e^{-[V_{SI}(R-\Delta R) - E_T]\delta\tau}, \end{aligned} \quad (49)$$

where V_{SI} is the spin/isospin-independent part of the interaction. We then sample one of the above choices according to the ratios w_i . Finally, the total weight of the new configuration is given by

$$W = \frac{1}{4} \sum_i w_i, \quad (50)$$

and W is used for branching as in the standard DMC method [1].

E. Observables

The expectation value of an observable \mathcal{O} is calculated by using the sampled configurations $R_i S_i$ as

$$\langle \mathcal{O}(\tau) \rangle = \frac{\sum_i \frac{\langle R_i S_i | \mathcal{O} | \Psi_T \rangle}{W} \frac{W}{\langle R_i S_i | \Psi_T \rangle}}{\sum_i \frac{W}{\langle R_i S_i | \Psi_T \rangle}}. \quad (51)$$

The above expression is valid only for observables that commute with the Hamiltonian. For other observables, such as radii and densities, expectation values are often calculated from

mixed estimates

$$\langle \mathcal{O}(\tau) \rangle \approx 2 \frac{\langle \Psi_T | \mathcal{O} | \Psi(\tau) \rangle}{\langle \Psi_T | \Psi(\tau) \rangle} - \frac{\langle \Psi_T | \mathcal{O} | \Psi_T \rangle}{\langle \Psi_T | \Psi_T \rangle}, \quad (52)$$

where the first term corresponds to the DMC expectation value and the second term is the VMC one. Equation (52) is valid for diagonal matrix elements, but it can be generalized to the case of off-diagonal matrix elements, e.g., in transition matrix elements between different initial and final states (see Ref. [42]).

Note that the extrapolation above is small for accurate trial wave functions. This is the case, for instance, for closed-shell nuclei and single operators. For open-shell systems, particularly for halo nuclei, the information encoded in the trial wave function may not be as accurate as that for simpler systems. This can result in a non-negligible extrapolation of the mixed expectation value. An example of this behavior is provided by the nuclear radius, the VMC expectation value of which is typically larger than the DMC one for open-shell systems. One way to reduce the extrapolation of the mixed estimate for the radius is to use a penalty function during the optimization of the variational parameters in the trial wave function. This penalty function sets a constraint on the VMC radius so as to adjust its expectation value close to the DMC estimate, thus reducing the extrapolation.

F. Constrained and unconstrained evolution

The fact that the weight W is always real and positive and that Ψ_T is complex makes the denominator of Eq. (51) average quickly to zero. This is the well known sign problem in DMC methods. One way to avoid the sign problem is to use a constraint during the imaginary-time evolution. In practice, a configuration is given zero weight (thus it is dropped during branching) if its real part changes sign.

In our implementation of the AFDMC method, we follow Ref. [43]. In sampling the propagator, we calculate the weights w_i of Eq. (49) as

$$\frac{\langle \Psi_G | (R', S'(X)) \rangle}{\langle \Psi_G | RS \rangle} \rightarrow \text{Re} \left\{ \frac{\langle \Psi_T | (R', S'(X)) \rangle}{\langle \Psi_T | RS \rangle} \right\}, \quad (53)$$

and we then apply the constraint by assigning zero weight to a move that results in a negative ratio. This is analogous to the constrained-path approximation [44], but for complex wave functions and propagators.

This constrained evolution does not suffer a sign problem, but it makes the final result dependent on the choice of Ψ_T . Moreover, it implies that the calculated energy is not necessarily an upper bound to the true ground-state energy, as is the case of the fixed-node approximation in real space [41,45].

The results given by the constrained evolution can be improved by releasing the constraint and following the unconstrained evolution. After a set of configurations is generated using the constraint, the guiding function is taken as

$$\langle \Psi_G | RS \rangle = \text{Re}\{\langle \Psi_G | RS \rangle\} + \alpha \text{Im}\{\langle \Psi_G | RS \rangle\}, \quad (54)$$

where α is a small arbitrary constant. This ensures that the ratio in the weights w_i of Eq. (49) is always positive and

real. The propagation continues then according to the modified $\langle \Psi_G | RS \rangle$, and observables are calculated as before according to Eq. (51). In several cases the expectation value $\langle O \rangle$ reaches a stable value independent of imaginary time before the signal-to-noise ratio goes to zero, and the result is exact within the statistical uncertainty. This is the case for light systems, $A \leq 4$. For larger nuclei the variance grows much faster as a function of the imaginary time, so that the unconstrained evolution cannot always be followed until $\langle O \rangle$ reaches a plateau. In these cases, the final result is extrapolated using an exponential fit as in Ref. [40]. We found that a single-exponential form with free-sign coefficients yields the most stable fits in our case. Such a form has been used to obtain all the quoted results. Examples of unconstrained evolution are provided in Sec. VIA.

V. TRIAL WAVE FUNCTION

The AFDMC trial wave function we use takes the form

$$\begin{aligned} \langle RS | \Psi \rangle = \langle RS | & \prod_{i < j} f_{ij}^1 \prod_{i < j < k} f_{ijk}^{3c} \\ & \times \left[\mathbb{1} + \sum_{i < j} \sum_{p=2}^6 f_{ij}^p \mathcal{O}_{ij}^p f_{ij}^{3p} + \sum_{i < j < k} U_{ijk} \right] | \Phi \rangle_{J^\pi, T}, \end{aligned} \quad (55)$$

where $|RS\rangle$ represents the sampled $3A$ spatial coordinates and the $4A$ spin/isospin amplitudes for each nucleon, and the pair correlation functions $f_{ij}^{p=1,6} \equiv f^{p=1,6}(r_{ij})$ are obtained as the solution of Schrödinger-like equations in the relative distance between two particles, as explained in Ref. [1]. The two spin/isospin-independent functions f_{ijk}^{3c} and f_{ij}^{3p} are defined as

$$\begin{aligned} f_{ijk}^{3c} &= 1 + q_1^c \mathbf{r}_{ij} \cdot \mathbf{r}_{ik} \mathbf{r}_{ji} \cdot \mathbf{r}_{jk} \mathbf{r}_{ki} \cdot \mathbf{r}_{kj} e^{-q_2^c(r_{ij}+r_{ik}+r_{jk})}, \\ f_{ij}^{3p} &= \prod_k [1 - q_1^p (1 - \mathbf{r}_{ik} \cdot \mathbf{r}_{jk}) e^{-q_2^p(r_{ij}+r_{ik}+r_{jk})}], \end{aligned} \quad (56)$$

and they are introduced to reduce the strength of the spin/isospin-dependent pair correlation functions when other particles are nearby [40]. Finally, three-body spin/isospin-dependent correlations are also included as

$$U_{ijk} = \sum_n \epsilon_n V_{ijk}^n(\alpha_n r_{ij}, \alpha_n r_{ik}, \alpha_n r_{jk}), \quad (57)$$

where the terms V_{ijk}^n are the same as the $3N$ interactions of Eq. (7), ϵ_n are potential quenching factors, and α_n are coordinate scaling factors. In the correlations above, we include the four terms $V_a^{2\pi, P}$, $V^{2\pi, S}$, V_D , and V_E . $V_c^{2\pi, P}$ can also be implemented in the trial wave function, but since its structure involves three-body spin/isospin operators, its inclusion results in a severely larger computational cost.

The term $|\Phi\rangle$ is taken as a shell-model-like wave function. It consists of a sum of Slater determinants constructed using single-particle orbitals,

$$\langle RS | \Phi \rangle_{J^\pi, T} = \sum_n c_n \left[\sum \mathcal{C}_{JM} \mathcal{D}\{\phi_\alpha(\mathbf{r}_i, s_i)\}_{J, M} \right]_{J^\pi, T}, \quad (58)$$

where \mathbf{r}_i are the spatial coordinates of the nucleons, and s_i represents their spinor. J is the total angular momentum, M its projection, T the total isospin, and π the parity. The determinants \mathcal{D} are coupled with Clebsch-Gordan coefficients C_{JM} in order to reproduce the experimental total angular momentum, total isospin, and parity (J^π, T). The c_n are variational parameters multiplying different components having the same quantum numbers. Each single-particle orbital ϕ_α consists of a radial function multiplied by the spin/isospin trial states

$$\phi_\alpha(\mathbf{r}_i, s_i) = \Phi_{nj}(r_i)[Y_{l,m_l}(\hat{\mathbf{r}}_i)\chi_\gamma(s_i)]_{j,m_j}, \quad (59)$$

where the spherical harmonics $Y_{l,m_l}(\hat{\mathbf{r}}_i)$ are coupled to the spin state $\chi_\gamma(s_i)$ in order to have single-particle orbitals in the j basis. The radial parts $\Phi(r)$ are obtained from the bound-state solutions of the Woods-Saxon wine-bottle potential

$$v(r) = V_s \left[\frac{1}{1 + e^{(r-r_s)/a_s}} + \alpha_s e^{-(r/\rho_s)^2} \right], \quad (60)$$

where the five parameters V_s, r_s, a_s, α_s , and ρ_s can be different for orbitals belonging to different states, such as $1S_{1/2}, 1P_{3/2}, 1P_{1/2}, \dots$, and they are optimized in order to minimize the variational energy. Finally, the spin/isospin trial states are represented in the $|p\rangle, |p\rangle, |n\rangle, |n\rangle$ basis ($|\chi_{\gamma=1,4}\rangle$). The spinors are specified as

$$|s_i\rangle \equiv \begin{pmatrix} a_i \\ b_i \\ c_i \\ d_i \end{pmatrix} = a_i|p\rangle + b_i|p\rangle + c_i|n\rangle + d_i|n\rangle, \quad (61)$$

and the trial spin/isospin states are taken to be

$$\begin{aligned} \chi_1(s_i) &= \langle s_i | \chi_1 \rangle = \langle s_i | (1, 0, 0, 0) \rangle = a_i, \\ \chi_2(s_i) &= \langle s_i | \chi_2 \rangle = \langle s_i | (0, 1, 0, 0) \rangle = b_i, \\ \chi_3(s_i) &= \langle s_i | \chi_3 \rangle = \langle s_i | (0, 0, 1, 0) \rangle = c_i, \\ \chi_4(s_i) &= \langle s_i | \chi_4 \rangle = \langle s_i | (0, 0, 0, 1) \rangle = d_i. \end{aligned} \quad (62)$$

Let us consider a system with K states. According to the definitions above, a single Slater determinant

$\mathcal{D} \equiv \mathcal{D}\{\phi_\alpha(\mathbf{r}_i, s_i)\}_{J,M}$ is constructed as

$$\mathcal{D} = \begin{vmatrix} a_1\phi_1(\mathbf{r}_1) & a_2\phi_1(\mathbf{r}_2) & \cdots & a_A\phi_1(\mathbf{r}_A) \\ a_1\phi_2(\mathbf{r}_1) & a_2\phi_2(\mathbf{r}_2) & \cdots & a_A\phi_2(\mathbf{r}_A) \\ \vdots & \vdots & \ddots & \vdots \\ b_1\phi_1(\mathbf{r}_1) & b_2\phi_1(\mathbf{r}_2) & \cdots & b_A\phi_1(\mathbf{r}_A) \\ b_1\phi_2(\mathbf{r}_1) & b_2\phi_2(\mathbf{r}_2) & \cdots & b_A\phi_2(\mathbf{r}_A) \\ \vdots & \vdots & \ddots & \vdots \\ d_1\phi_1(\mathbf{r}_1) & d_2\phi_1(\mathbf{r}_2) & \cdots & d_A\phi_1(\mathbf{r}_A) \\ \vdots & \vdots & \ddots & \vdots \\ d_1\phi_K(\mathbf{r}_1) & d_2\phi_K(\mathbf{r}_2) & \cdots & d_A\phi_K(\mathbf{r}_A) \end{vmatrix}. \quad (63)$$

For ^{16}O ($0^+, 0$), for instance, the number of states is four: one $1S_{1/2}$, two $1P_{3/2}$, and one $1P_{1/2}$. Each of them can accommodate two spins and two isospin states, and the full $\langle RS | \Phi \rangle_{0^+, 0}$ wave function can be written as a single Slater determinant. For open-shell systems, instead, many Slater determinants need to be included in order to have a good trial wave function with the proper (J^π, T). For $A = 6$ systems, e.g., including single-particle orbitals up to the sd shell, there are ten possible states: one $1S_{1/2}$, two $1P_{3/2}$, one $1P_{1/2}$, three $1D_{5/2}$, two $1D_{3/2}$, and one $2S_{1/2}$. These can be combined in nine different Slater determinants in order to have the ^6He ($0^+, 1$) wave function, or in 32 Slater determinants to make ^6Li ($1^+, 0$). Finally, for ^{12}C ($0^+, 0$), by considering only $K = 4$ as for ^{16}O ($0^+, 0$), the number of Slater determinants needed to build a ($0^+, 0$) wave function is already 119, making it computationally challenging to include sd -shell orbitals for $A = 12$.

The trial wave function of Eq. (55) contains a sum over pair correlation functions, meaning that only one pair of nucleons ij is correlated at a time (linear correlations). This is different from the GFMC wave function [1], where all pairs are correlated at the same time. In the AFDMC method, this same construction would, however, forbid the application of the Hubbard-Stratonovich transformation, justifying the choice of Eq. (55). An improved AFDMC two-body wave function could include linear and quadratic pair correlations:

$$\langle RS | \Psi \rangle_{2b} = \langle RS | \prod_{i < j} f_{ij}^1 \left[1 + \sum_{i < j} \sum_{p=2}^6 f_{ij}^p \mathcal{O}_{ij}^p + \sum_{i < j} \sum_{p=2}^6 f_{ij}^p \mathcal{O}_{ij}^p \sum_{\substack{k < l \\ ij \neq kl}} \sum_{q=2}^6 f_{kl}^q \mathcal{O}_{kl}^q \right] | \Phi \rangle_{J^\pi, T}, \quad (64)$$

where the sum over kl includes all nucleon pairs except when $k = i$ and $l = j$. The $f_{ij}^{p,q}$ functions are solved for as before, and the operators $\mathcal{O}_{ij}^{p,q}$ are the same as in Eq. (55). Although the two-body wave function of Eq. (64) contains all quadratic correlations, most of the relevant physics is captured with a subset of these correlations, corresponding to the action of the $\mathcal{O}_{ij}^{p,q}$ operators on four distinct particles (so-called independent pair correlations). Since these correlations never act on the same particle, all the $\mathcal{O}_{ij}^{p,q}$ operators commute, removing the need for an explicit symmetrization of the wave function.

Such a wave function could, in principle, improve the energy expectation value for large systems, but the computational cost of its evaluation is significantly higher than for a wave function with linear correlations only. In fact, the cost of computing expectation values of two-body operators on a two-body wave function of the form of Eq. (64) is proportional to A^4 for linear correlations, and to A^6 for quadratic correlations. For this reason in the present work we consider only linear two-body correlations in the wave function, and we present a test study of quadratic correlations in Sec. VIB.

TABLE I. ${}^4\text{He}$ ground-state energies for the AV6' potential and different trial wave functions (see text for details). C (U) refers to the constrained (unconstrained) evolution. Errors are statistical. Results are in MeV.

Energy	Simple w.f.	Full w.f.
E_{VMC}	-9.49(5)	-23.35(1)
$E_{\text{AFDMC}}^{\text{C}}$	-25.28(3)	-26.45(1)
$E_{\text{AFDMC}}^{\text{U}}$	-26.34(12)	-26.31(4)

VI. RESULTS

A. Test of constrained and unconstrained evolution

As introduced in Sec. IV F, the energy (and other observables) calculated with the AFDMC method during the constrained evolution is dependent on the choice of Ψ_T . This is shown in Table I where the energy of ${}^4\text{He}$ is calculated for the Argonne v'_6 (AV6') potential [34] employing different trial wave functions. Full w.f. refers to the wave function of Eq. (55) where all the two-body correlations are included. Simple w.f. is instead a simplified wave function where only $p = 1,5$ operators are included in the two-body correlations, the strength of the latter ($\mathcal{O}_{ij}^5 = S_{ij}$) being artificially reduced by a factor 3 after the optimization process. At the variational level it is evident how the simplified wave function is not the optimal choice for Ψ_T , as the energy expectation value is much higher than for the fully optimized wave function. For both choices of Ψ_T , the constrained evolution reduces the binding energy, moving towards the GFMC reference value for the same potential (see Table II), but the results are still inconsistent. It is only the unconstrained evolution that brings the results for both wave functions in agreement within statistical errors. This is also shown in Fig. 1, where the AFDMC energy is plotted as a function of imaginary time for the unconstrained evolution.

We report in Table II the constrained and unconstrained energies for $A = 3,4,6$ employing the AV6' potential, in comparison with the GFMC results for the same interaction [34]. It is interesting to note that constrained energies do not always satisfy the variational principle, as anticipated in Sec. IV F. This is seen, e.g., in ${}^3\text{H}$ and ${}^4\text{He}$, for which the constrained energy is below the GFMC prediction, considered to be the exact solution for the given potential. However, once the unconstrained evolution is performed, the AFDMC and GFMC results agree within 1% or less.

In Figs. 2 and 3 we show two examples of unconstrained calculation for larger systems, ${}^6\text{He}$ and ${}^{16}\text{O}$ respectively,

TABLE II. Ground state energies for $A = 3,4,6$ employing the AV6' potential. Errors are statistical. Results are in MeV.

${}^A Z (J^\pi, T)$	$E_{\text{AFDMC}}^{\text{C}}$	$E_{\text{AFDMC}}^{\text{U}}$	E_{GFMC}
${}^3\text{H} (\frac{1}{2}^+, \frac{1}{2})$	-8.08(1)	-7.95(2)	-7.95(2)
${}^4\text{He} (0^+, 0)$	-26.45(1)	-26.31(4)	-26.15(2)
${}^6\text{Li} (1^+, 0)$	-28.09(4)	-28.26(10)	-28.37(4)

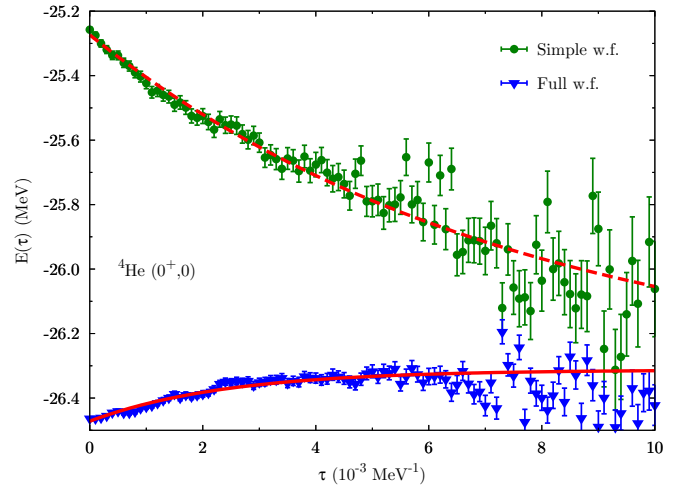


FIG. 1. Energy of ${}^4\text{He}$ as a function of imaginary time after releasing the constraint for the AV6' potential. The two data sets refer to the two different wave functions of Table I. Red lines are exponential fits to the Monte Carlo results.

employing realistic two- plus three-body interactions. We use the local chiral potential at N^2LO with cutoff $R_0 = 1.2$ fm for ${}^6\text{He}$ and $R_0 = 1.0$ fm for ${}^{16}\text{O}$. The employed wave functions include all two- and three-body correlations, and for ${}^6\text{He}$ we include single-particle orbitals up to the sd shell. In general, the larger the system, the shorter the imaginary-time evolution that can be followed before the variance becomes too large. This is particularly evident in ${}^{16}\text{O}$, for which the unconstrained evolution can be satisfactorily performed up to $2.5 \times 10^{-4} \text{ MeV}^{-1}$, compared to the $4 \times 10^{-4} \text{ MeV}^{-1}$ for ${}^6\text{He}$ of Fig. 2 with the same interaction, and to the $5 \times 10^{-3} \text{ MeV}^{-1}$ (10^{-2} MeV^{-1}) for ${}^4\text{He}$ (with AV6' of Fig. 1). For example, at $\tau = 2 \times 10^{-4} \text{ MeV}^{-1}$ the statistical error per nucleon is 0.01 MeV for ${}^4\text{He}$ and ${}^6\text{Li}$, and 0.19 MeV for ${}^{16}\text{O}$. This is a direct consequence of the quality of the employed wave

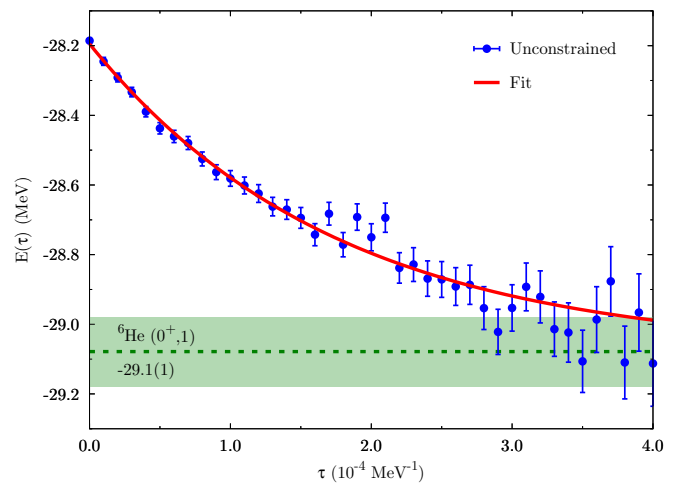


FIG. 2. ${}^6\text{He}$ unconstrained evolution for the local chiral potential at N^2LO ($E\tau$) with cutoff $R_0 = 1.2$ fm. Data points refer to the expectation value of H' , Eq. (44).

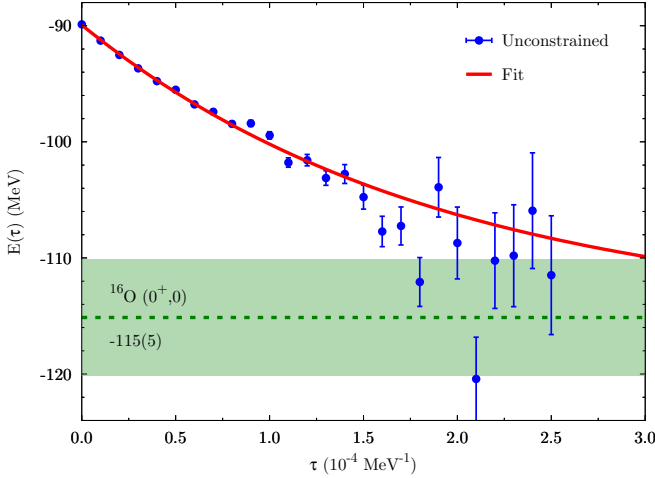


FIG. 3. ^{16}O unconstrained evolution for the local chiral potential at N^2LO ($E\tau$) with cutoff $R_0 = 1.0$ fm. Data points refer to the expectation value of H' , Eq. (44).

function. For small nuclei, the wave function of Eq. (55) provides a good description of the system, and the energy expectation value of the constrained evolution is already close to the expected result. In ^6He the difference between the constrained and unconstrained energy is of the order of 1 MeV, roughly 3% of the final result. In ^{16}O , instead, the constrained energy is higher, and the unconstrained evolution lowers its value by about 25 MeV, $\approx 22\%$ of the total energy. This could be improved by employing more sophisticated wave functions including higher order correlations, such as in Eq. (64), and/or using more refined techniques to perform the unconstrained evolution. Studies along these directions are underway.

B. Test of quadratic two-body correlations

The results presented in the previous section are obtained using a trial wave function of the form of Eq. (55), i.e., by retaining only two-body linear correlations in $\langle RS|\Psi\rangle$. We present in Table III a test study on the effect of including quadratic correlations in the wave function on the energy expectation value. The energy expectation values for the constrained evolution have been calculated for ^4He , ^{16}O , and symmetric nuclear matter (SNM) with 28 particles in a box with periodic boundary conditions at saturation density $\rho_0 = 0.16 \text{ fm}^{-3}$. We use the AV6' potential with no Coulomb interaction for all the systems. Results are shown for the linear, independent pair, and full quadratic two-body correlations.

TABLE III. Energy per nucleon (in MeV) for ^4He , ^{16}O , and SNM at ρ_0 . The employed potential is AV6'. No Coulomb interaction is considered here. Results are shown for the linear, independent pair, and full quadratic two-body correlations. Errors are statistical.

System	Linear	Ind. pair	Quadratic
^4He	-6.79(1)	-6.81(1)	-6.78(1)
^{16}O	-7.23(6)	-7.59(9)	-7.50(9)
SNM	-13.92(6)	-14.80(7)	-14.70(11)

Though there is little difference in ^4He , the constrained energies for both ^{16}O and SNM are lower when employing quadratic correlations, particularly for SNM. In ^{16}O the energy gain for the constrained evolution is only $\approx 0.3(1)$ MeV/A, while in SNM this value increases up to $\approx 0.8(1)$ MeV/A. Within statistical uncertainties, no difference in the results is found between independent pair and full quadratic correlations, though the latter have a higher computational cost. Note that the variational parameters in the trial wave function of Eq. (64) were re-optimized for ^4He . In the case of ^{16}O and SNM, instead, due to the cost of optimizing such parameters using the full wave function of Eq. (64), we used the same parameters obtained for the linear wave function of Eq. (55).

C. Fit of the three-body interaction

The three-body interaction, which appears naturally in the chiral expansion at N^2LO , introduces two additional LECs that need to be fit to experimental data. The choice considered here is to fit the LECs c_D and c_E , multiplying the intermediate- and short-range parts of the $3N$ interaction respectively [see Eq. (14)], to two uncorrelated observables as in Ref. [23]: the binding energy of ^4He and n - α scattering P -wave phase shifts. This choice probes properties of light nuclei (the ^4He binding energy) while also providing a handle on spin-orbit splitting via the splitting in the two P -wave n - α phase shifts. Furthermore, the n - α system is the lightest nuclear system presenting three interacting neutrons. It follows that this choice constrains c_D and c_E well, and also probes $T = 3/2$ physics.

The detailed fitting procedure is reported in Ref. [23], where different parametrizations of the three-body force for different cutoffs were explored. No fit for the $E\parallel$ parametrization and the softer cutoff $R_0 = 1.2$ fm was reported at that time. However, in Ref. [33] a significant overbinding of ^{16}O was found for this softer cutoff and the $E\tau$ parametrization of the $3N$ interaction. Locally regulated chiral interactions spoil the Fierz ambiguity typically exploited to allow the selection of one of six operators in the contact interaction V_E ; see Refs. [23,47] for details. This means that observables will depend on the parametrization of the $3N$ interaction and, as suggested in Ref. [23], this is especially true for larger or more dense nuclear systems. Reference [23] also showed that the $E\tau$ parametrization was the most attractive of the two parametrizations, while the $E\parallel$ parametrization was the least attractive. Therefore, it becomes important to consider now the $E\parallel$ parametrization with the softer cutoff $R_0 = 1.2$ fm. This combination is thus explored in this work, together with the $E\parallel$ parametrization for the $R_0 = 1.0$ fm cutoff, and the $E\tau$ parametrization for both cutoffs. In Fig. 4 we report the P -wave n - α phase shifts for the four different combinations of operator structure and cutoff considered in this work. The corresponding values of c_D and c_E are shown in Table IV.

D. Test of the three-body calculation

The energies reported in Figs. 2 and 3 correspond to the expectation values of the effective Hamiltonian H' , Eq. (44). These need to be adjusted with the perturbative correction of Eq. (46)—also extracted from the unconstrained evolution—in

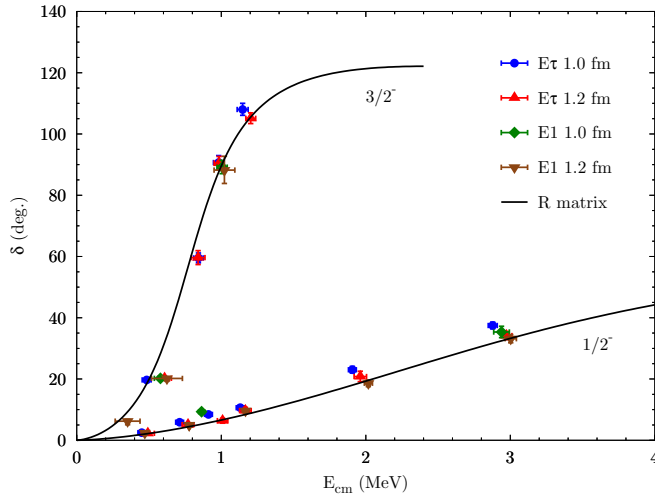


FIG. 4. P -wave n - α elastic scattering phase shifts compared to an R -matrix analysis of experimental data [46].

order to obtain the final results reported in Tables VIII and IX. Once the optimal set of parameters α_i is found, these corrections are small, almost consistent with zero within Monte Carlo statistical uncertainties, as shown in Table V.

The final result $\langle H \rangle$ is, however, nearly independent of variations of the α_i parameters, even for larger systems. This is shown in Table VI where the α_i are arbitrarily changed in ^{16}O within 5–10% with respect to the optimal values, given in the first row for each cutoff. This results in $\lesssim 4\%$ variations of the total energy, compatible with the overall Monte Carlo statistical uncertainties. Note that, in order to save computing time, this test has been done using the constrained evolution. However, the optimal constrained expectation values $\langle V_{\text{pert}} \rangle$ are consistent with the unconstrained ones of Table V.

Unless specified otherwise, in the following, all ground-state energies correspond to the final expectation value $\langle H \rangle$, extracted from the unconstrained Monte Carlo results for $\langle H' \rangle$ with an exponential fit, and adjusted with the perturbative correction of Eq. (46) when $3N$ forces are employed.

E. Ground-state energies and charge radii

We consider local chiral Hamiltonians at leading-order (LO), next-to-leading-order (NLO), and $N^2\text{LO}$, the latter including both two- and three-body forces. At each order we can assign theoretical uncertainties to observables coming from the truncation of the chiral expansion; see, e.g., Ref. [48]. For an observable X at $N^2\text{LO}$, the theoretical uncertainty is

TABLE IV. LECs c_D and c_E for different cutoffs and parametrizations of the $3N$ force.

$3N$	R_0 (fm)	c_D	c_E
$E\tau$	1.0	0.0	-0.63
	1.2	3.5	0.09
$E1$	1.0	0.5	0.62
	1.2	-0.75	0.025

TABLE V. Energy expectation values of Eq. (46) for $A \geq 6$. Errors are statistical. Results are in MeV.

$^A Z (J^\pi, T)$	$3N$	R_0 (fm)	$\langle H' \rangle$	$\langle V_{\text{pert}} \rangle$	$\langle H \rangle$
$^6\text{He} (0^+, 1)$	$E\tau$	1.0	-28.3(4)	0.1(2)	-28.4(4)
		1.2	-29.1(1)	0.2(1)	-29.3(1)
	$E1$	1.0	-28.5(5)	-0.3(2)	-28.2(5)
		1.2	-27.3(3)	0.1(2)	-27.4(4)
$^6\text{Li} (1^+, 0)$	$E\tau$	1.0	-31.2(4)	0.3(3)	-31.5(5)
		1.2	-31.9(3)	0.4(1)	-32.3(3)
	$E1$	1.0	-30.9(4)	-0.2(2)	-30.7(4)
		1.2	-30.0(3)	-0.1(2)	-29.9(4)
$^{12}\text{C} (0^+, 0)$	$E\tau$	1.0	-75(2)	3(1)	-78(3)
$^{16}\text{O} (0^+, 0)$	$E\tau$	1.0	-115(5)	2(1)	-117(5)
		1.2	-265(25)	-2(6)	-263(26)
	$E1$	1.0	-114(6)	1(2)	-115(6)
		1.2	-113(5)	-2(2)	-111(5)

obtained as

$$\Delta X^{N^2\text{LO}} = \max(Q^4 \times |X^{\text{LO}}|, Q^2 \times |X^{\text{NLO}} - X^{\text{LO}}|, Q \times |X^{N^2\text{LO}} - X^{\text{NLO}}|), \quad (65)$$

where we take $Q = m_\pi/\Lambda_b$ with $m_\pi \approx 140$ MeV and $\Lambda_b = 600$ MeV, as in Ref. [33].

The expectation value of the charge radius is derived from the point-proton radius using the relation

$$\langle r_{\text{ch}}^2 \rangle = \langle r_{\text{pt}}^2 \rangle + \langle R_p^2 \rangle + \frac{A-Z}{Z} \langle R_n^2 \rangle + \frac{3\hbar^2}{4M_p^2 c^2}, \quad (66)$$

where r_{pt} is the calculated point-proton radius, $\langle R_p^2 \rangle = 0.770(9)$ fm 2 [49] the proton radius, $\langle R_n^2 \rangle = -0.116(2)$ fm 2 [49] the neutron radius, and $(3\hbar^2)/(4M_p^2 c^2) \approx 0.033$ fm 2 the Darwin-Foldy correction [50]. For ^6He a spin-orbit correction $\langle r_{\text{so}}^2 \rangle = -0.08$ fm 2 [51] is also included. The point-nucleon

TABLE VI. Contributions to the energy expectation value of Eq. (46) in ^{16}O . The parametrization $E\tau$ of the $3N$ force is used for different cutoffs. $\langle V_{\text{pert}} \rangle$ is extracted from a mixed estimate, as in Eq. (52). For each cutoff, the first line represents the optimal choice for α_i . Energies (in MeV) are the result of the constrained evolution. Errors are statistical.

R_0 (fm)	$(\alpha_1, \alpha_2, \alpha_3)$	$\langle H' \rangle$	$\langle V_{\text{pert}} \rangle$	$\langle H \rangle$
1.0	(2.05, -3.80, -0.95)	-90.0(3)	1.8(5)	-91.8(6)
	(2.50, -3.30, -1.20)	-125.1(6)	-33.9(8)	-92.2(1.0)
	(1.95, -4.00, -0.90)	-83.3(2)	5.9(9)	-89.2(1.0)
	(1.80, -4.20, -0.85)	-75.6(3)	13.9(1.4)	-89.4(1.5)
1.2	(1.80, 0.45, 8.00)	-171(2)	-2(1)	-169(2)
	(1.90, 0.50, 8.50)	-197(3)	-25(2)	-172(3)
	(1.70, 0.40, 7.50)	-147(1)	15(1)	-162(1)

TABLE VII. Ground-state energies and charge radii for $A = 3, 4$ employing local chiral potentials at N^2 LO. The $E\tau$ parametrization of the $3N$ force is used. Errors are statistical. GFMC results are from Refs. [23,27].

Nucleus ${}^A Z (J^\pi, T)$	Cutoff R_0 (fm)	Potential	AFDMC		GFMC	
			E (MeV)	r_{ch} (fm)	E (MeV)	r_{ch} (fm)
${}^3\text{H} (\frac{1}{2}^+, \frac{1}{2})$	1.0	NN	-7.54(4)	1.75(2)	-7.55(1)	1.78(2)
		$3N E\tau$	-8.33(7)	1.72(2)	-8.34(1)	1.72(3)
	1.2	NN	-7.76(3)	1.74(2)	-7.74(1)	1.75(2)
		$3N E\tau$	-8.27(5)	1.73(2)	-8.35(4)	1.72(4)
${}^3\text{He} (\frac{1}{2}^+, \frac{1}{2})$	1.0	NN	-6.89(5)	2.02(2)	-6.78(1)	2.06(2)
		$3N E\tau$	-7.55(8)	1.96(2)	-7.65(2)	1.97(2)
	1.2	NN	-7.12(3)	1.98(2)	-7.01(1)	2.01(1)
		$3N E\tau$	-7.64(4)	1.95(5)	-7.63(4)	1.97(1)
${}^4\text{He} (0^+, 0)$	1.0	NN	-23.96(8)	1.72(2)	-23.72(1)	1.73(1)
		$3N E\tau$	-27.64(13)	1.68(2)	-28.30(1)	1.65(2)
	1.2	NN	-25.17(5)	1.69(1)	-24.86(1)	1.69(1)
		$3N E\tau$	-28.37(8)	1.65(1)	-28.30(1)	1.64(1)

radius r_{pt} is calculated as

$$\langle r_N^2 \rangle = \frac{1}{\mathcal{N}} \langle \Psi | \sum_i \mathcal{P}_{N_i} |\mathbf{r}_i - \mathbf{R}_{\text{cm}}|^2 | \Psi \rangle, \quad (67)$$

where \mathbf{R}_{cm} is the coordinate of the center of mass of the system, \mathcal{N} is the number of protons or neutrons, and

$$\mathcal{P}_{N_i} = \frac{1 \pm \tau_{z_i}}{2} \quad (68)$$

is the projector operator onto protons or neutrons. The charge radius is a mixed expectation value, and it requires the calculation of both VMC and DMC point-proton radii, according to Eq. (52). Regardless of the employed optimization of the variational wave function (free or constrained), the extrapolation of the mixed estimate (r_{ch}^2) is small, and the final results for different optimizations typically agree within statistical uncertainties.

The ground-state energies and charge radii for light systems ($A = 3, 4$) employing local chiral potential at N^2 LO are shown in Table VII. Results with ($E\tau$ parametrization) and without the $3N$ force are shown for different choices of the cutoff R_0 . For all the $s_{1/2}$ systems we used the same parameters α_i for the propagation of the $3N$ force, determined in order to minimize the perturbative correction of Eq. (46). The agreement with the GFMC results of Ref. [23,28], where the $3N$ interactions are fully included in the propagation, is within a few percent both at the two- and three-body levels, providing a good benchmark for the AFDMC propagation technique described in Sec. IV C.

In Fig. 5 we present the ground-state energies per nucleon of nuclei with $3 \leq A \leq 16$ for cutoffs $R_0 = 1.0$ and $R_0 = 1.2$ fm, respectively. Results at LO, NLO, and N^2 LO for both $E\tau$ and $E1$ parametrizations of the $3N$ force are shown. Error bars are estimated by including both the Monte Carlo uncertainties and the errors given by the truncation of the chiral

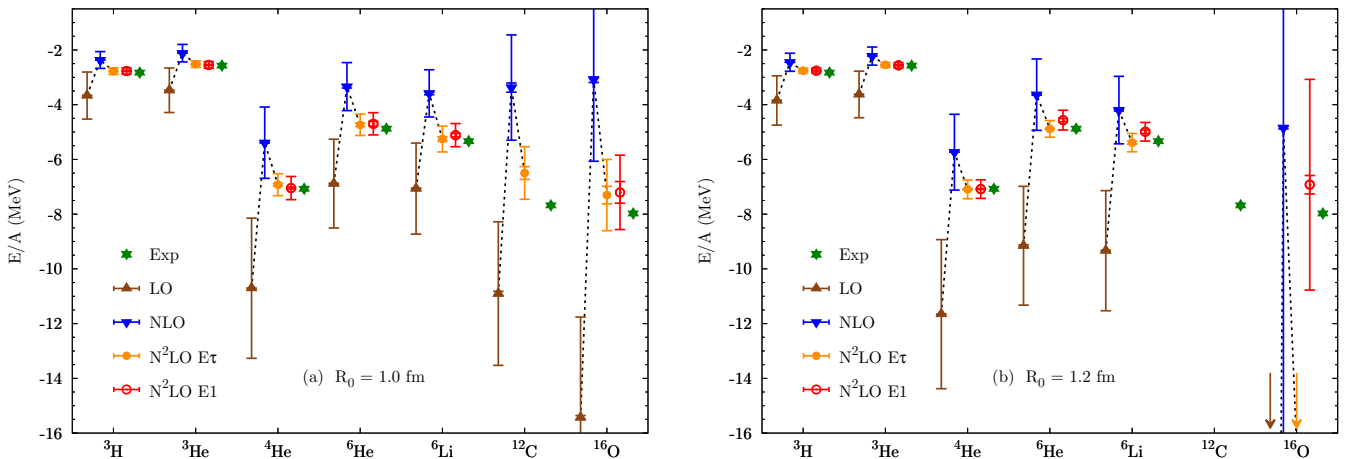


FIG. 5. Ground-state energies per nucleon for $3 \leq A \leq 16$ with local chiral potentials: (a) $R_0 = 1.0$ fm cutoff (left panel), (b) $R_0 = 1.2$ fm cutoff (right panel). Results at different orders of the chiral expansion and for different $3N$ parametrizations are shown. Smaller error bars (indistinguishable from the symbols up to $A = 6$) indicate the statistical Monte Carlo uncertainty, while larger error bars are the uncertainties from the truncation of the chiral expansion. LO and N^2 LO $E\tau$ results for ${}^{16}\text{O}$ with $R_0 = 1.2$ fm are outside the displayed energy region. Updated from Ref. [33].

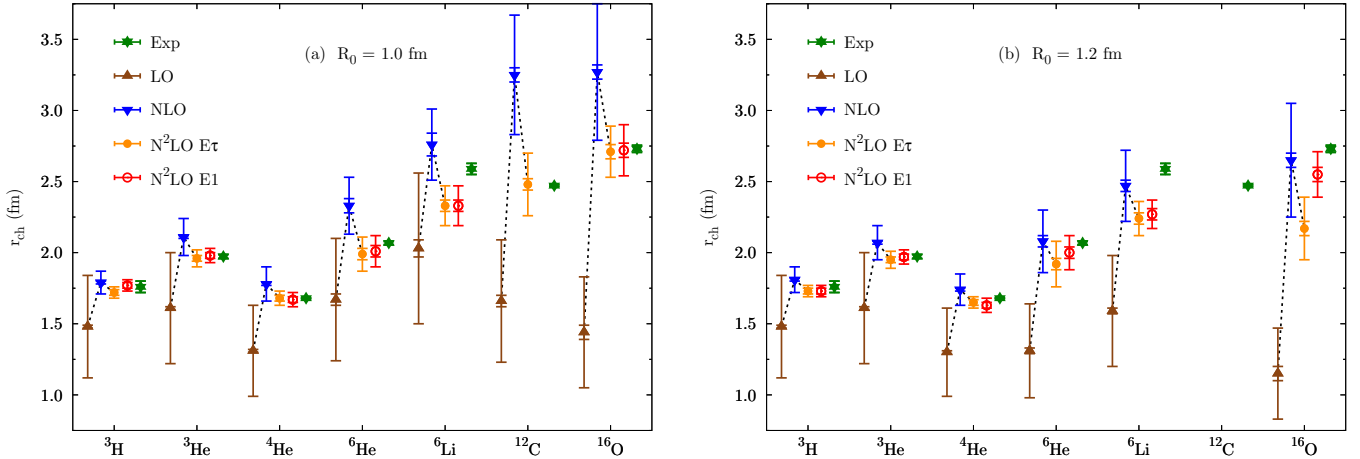


FIG. 6. Charge radii for $3 \leq A \leq 16$ with local chiral potentials: (a) $R_0 = 1.0$ fm cutoff (left panel), (b) $R_0 = 1.2$ fm cutoff (right panel). The legend and error bars are as in Fig. 5. Updated from Ref. [33].

expansion, the latter being the dominant ones. For the harder interaction ($R_0 = 1.0$ fm), the predicted binding energies at N²LO are in good agreement with experimental data all the way up to $A = 16$. No differences, within theoretical uncertainties, are found for the two different parametrizations of the $3N$ force.

¹²C in the $E\tau$ parametrization is slightly underbound. This is most likely a consequence of the employed wave function that results in a too high energy for the constrained evolution. This could be due to the complicated clustering structure of ¹²C not included in Ψ_T , which would require a much longer unconstrained propagation to filter out the corresponding low excitations from Ψ_T . For $A = 6$ the wave function is constructed using up to sd -shell single-particle orbitals. For ¹²C, instead, coupling p -shell orbitals only already results in a sum of 119 Slater determinants. Including orbitals in the sd -shell could in principle result in a better wave function for this open-shell system, but it will sizably increase the number of determinants to consider, making the calculation prohibitively time consuming. Another possible improvement would be to include quadratic terms in the pair correlations, as shown in Eq. (64). However, first attempts in ¹⁶O lead to just a $\approx 6(2)$ MeV reduction of the total energy in a simplified scenario (see Table III), with a noticeably increased computational cost.

For the softer interaction ($R_0 = 1.2$ fm), NLO and in particular LO results are typically more bound compared to the $R_0 = 1.0$ fm case. Both parametrizations of the $3N$ force make the N²LO energies compatible with the experimental values up to $A = 6$, and consistent with those obtained with the hard potential.

For the heaviest system considered here, ¹⁶O, the picture is quite different. At LO, the system is dramatically overbound (≈ -1 GeV), which would imply very large theoretical uncertainties at NLO and N²LO coming from the prescription of Eq. (65). Within these uncertainties, NLO and N²LO two-body energies are compatible with the corresponding results for the hard interaction (see Tables VIII and IX). However, the contribution of the $3N$ force at N²LO largely depends upon

the employed operator structure. The $E\tau$ parametrization for the soft potential is very attractive, adding almost 10 MeV per nucleon to the total energy, and thus predicting a significant overbinding with a ground-state energy of ≈ -260 MeV. The $E1$ parametrization is instead less attractive, resulting in ≈ 0.30 MeV per nucleon more binding with respect to the two-body case, compatible with the energy expectation values for the hard potential.

Figure 6 shows the charge radii at different orders of the chiral expansion and for different cutoffs and parametrizations of the $3N$ force. The agreement with experimental data for the hard interaction at N²LO is remarkably good all the way up to oxygen. One exception is ⁶Li, for which the charge radius is somewhat underpredicted. However, a similar conclusion is found in GFMC calculations employing the AV18+IL7 potential, where charge radii of lithium isotopes are underestimated [1].

For the soft interaction, the description of charge radii resembles order by order that for the hard potential up to $A = 6$, with the N²LO results in agreement with experimental data, except for ⁶Li (also shown in Table VII). The picture changes again for $A = 16$. The charge radius of ¹⁶O turns out to be close to 2.2 fm with the $E\tau$ parametrization of the $3N$ force, smaller than that of ⁶Li for the same potential, but consistent with the significant overbinding predicted for $A = 16$. The oxygen charge radius for the $E1$ parametrization is instead closer to the experimental value.

The details of LO, NLO, and N²LO calculations for $A \geq 6$ are reported in Tables VIII and IX for $R_0 = 1.0$ and $R_0 = 1.2$ fm, respectively. Results for the constrained and unconstrained evolution energies are both shown, together with the charge radii. Both Monte Carlo uncertainties and theoretical errors coming from the truncation of the chiral expansion are reported (where available). At N²LO the two-body energy is shown together with that of the two different parametrizations of the $3N$ force ($E\tau$ and $E1$).

The full calculation of ¹²C at N²LO required on the order of 10^6 CPU hours (on Intel Broadwell cores at 2.1 GHz) for a single cutoff (1.0 fm) and $3N$ parametrization ($E\tau$). Due to

TABLE VIII. Ground-state energies and charge radii for $A \geq 6$ with local chiral potentials. Results at different orders of the chiral expansion and for different $3N$ parametrizations are shown. Energy results are shown for both the constrained (E_C) and unconstrained (E) evolutions. The first error is statistical, the second is based on the EFT expansion uncertainty. The employed cutoff is $R_0 = 1.0$ fm. Experimental results are also shown.

${}^A Z (J^\pi, T)$	Potential	E_C (MeV)	E (MeV)	r_{ch} (fm)
${}^6\text{He} (0^+, 1)$	LO	-42.1(1)	-41.3(1)(9.6)	1.67(4)(39)
	NLO	-18.19(7)	-20.0(3)(5.0)	2.33(5)(15)
	$N^2\text{LO } NN$	-22.24(4)	-23.1(2)(1.2)	2.11(4)(5)
	$N^2\text{LO } 3N E\tau$	-26.58(6)	-28.4(4)(2.0)	1.99(4)(8)
	$N^2\text{LO } 3N E\mathbb{1}$	-26.33(8)	-28.2(5)(1.9)	2.01(4)(7)
	Exp		-29.3	2.068(11) [52]
${}^6\text{Li} (1^+, 0)$	LO	-42.8(1)	-42.4(1)(9.9)	2.03(6)(47)
	NLO	-19.2(2)	-21.5(3)(4.9)	2.76(8)(17)
	$N^2\text{LO } NN$	-24.3(1)	-25.5(4)(1.1)	2.46(4)(7)
	$N^2\text{LO } 3N E\tau$	-28.9(1)	-31.5(5)(2.3)	2.33(4)(10)
	$N^2\text{LO } 3N E\mathbb{1}$	-28.9(1)	-30.7(4)(2.1)	2.33(4)(10)
	Exp		-32.0	2.589(39) [53]
${}^{12}\text{C} (0^+, 0)$	LO	-131.5(2)	-131(1)(31)	1.66(4)(39)
	NLO	-31.1(2)	-41(2)(21)	3.25(5)(37)
	$N^2\text{LO } NN$	-63.5(2.4)	-66(3)(6)	2.66(4)(14)
	$N^2\text{LO } 3N E\tau$	-70.2(5)	-78(3)(9)	2.48(4)(18)
	$N^2\text{LO } 3N E\mathbb{1}$			
	Exp		-92.2	2.471(6) [54]
${}^{16}\text{O} (0^+, 0)$	LO	-251.7(2)	-247(1)(58)	1.44(3)(34)
	NLO	-37.3(2)	-49(2)(46)	3.27(5)(43)
	$N^2\text{LO } NN$	-72.8(2)	-87(3)(11)	2.76(5)(12)
	$N^2\text{LO } 3N E\tau$	-91.8(6)	-117(5)(16)	2.71(5)(13)
	$N^2\text{LO } 3N E\mathbb{1}$	-85.8(5)	-115(6)(15)	2.72(5)(11)
	Exp		-127.6	2.730(25) [55]

the high computational cost, no attempts were made for the $E\mathbb{1}$ parametrization of the $3N$ force or for the 1.2 fm cutoff.

As shown in Tables VIII and IX, the overbinding in ${}^{16}\text{O}$ happens only when the $3N$ force is included with the $E\tau$

parametrization for $R_0 = 1.2$ fm. The alternative combinations of three-body operators and cutoffs considered in this work predict instead binding energies compatible with the experimental value. A close look at the energy contributions

TABLE IX. Same as Table VIII but for the $R_0 = 1.2$ fm cutoff.

${}^A Z (J^\pi, T)$	Potential	E_C (MeV)	E (MeV)	r_{ch} (fm)
${}^6\text{He} (0^+, 1)$	LO	-55.65(6)	-54.9(2)(12.8)	1.31(2)(31)
	NLO	-21.41(6)	-21.8(1)(7.7)	2.08(4)(18)
	$N^2\text{LO } NN$	-24.25(5)	-24.3(1)(1.8)	2.02(4)(4)
	$N^2\text{LO } E\tau$	-28.37(5)	-29.3(1)(1.8)	1.92(4)(4)
	$N^2\text{LO } E\mathbb{1}$	-26.98(8)	-27.4(4)(1.8)	2.00(4)(4)
	Exp		-29.3	2.068(11) [52]
${}^6\text{Li} (1^+, 0)$	LO	-56.84(3)	-56.0(1)(13.1)	1.59(2)(37)
	NLO	-23.64(8)	-25.2(2)(7.2)	2.47(4)(21)
	$N^2\text{LO } NN$	-26.76(3)	-27.0(2)(1.7)	2.41(4)(5)
	$N^2\text{LO } E\tau$	-30.8(1)	-32.3(3)(1.7)	2.24(4)(6)
	$N^2\text{LO } E\mathbb{1}$	-29.2(1)	-29.9(4)(1.7)	2.29(4)(5)
	Exp		-32.0	2.589(39) [53]
${}^{16}\text{O} (0^+, 0)$	LO	-1158.8(5)	-1110(31)(259)	1.15(5)(27)
	NLO	-72.3(1)	-77.5(7)(240.8)	2.65(5)(35)
	$N^2\text{LO } NN$	-98.6(1)	-106(4)(56)	2.47(5)(8)
	$N^2\text{LO } E\tau$	-169(2)	-263(26)(56)	2.17(5)(11)
	$N^2\text{LO } E\mathbb{1}$	-99.5(4)	-111(5)(56)	2.55(5)(8)
	Exp		-127.6	2.730(25) [55]

TABLE X. Expectation value of the N^2 LO energy contributions in ${}^6\text{Li}$ and ${}^{16}\text{O}$. All energies (in MeV) are mixed estimates from the constrained evolution: $2 \langle \mathcal{O}_{\text{DMC}} \rangle - \langle \mathcal{O}_{\text{VMC}} \rangle$. Errors are statistical.

System	R_0 (fm)	Potential	E_{kin}	v_{ij}	$E_{\text{kin}} + v_{ij}$	V_{ijk}	$V^{2\pi,P}$	$V^{2\pi,S}$	V_D	V_E
${}^6\text{Li}$	1.0	NN	116.8(4)	-151.2(4)	-34.4(8)					
	1.0	$3N E\tau$	135.3(7)	-165.6(5)	-30.2(1.2)	-11.1(3)	-13.3(3)	-0.43(1)	0	2.67(2)
	1.0	$3N E\mathbb{1}$	135.5(6)	-165.8(6)	-30.3(1.2)	-11.3(2)	-13.3(2)	-0.42(1)	-0.89(2)	3.38(4)
	1.2	NN	110.3(3)	-145.4(3)	-35.1(6)					
	1.2	$3N E\tau$	129.3(6)	-160.1(5)	-30.8(1.1)	-11.8(3)	-6.1(2)	-0.39(1)	-4.6(1)	-0.63(1)
	1.2	$3N E\mathbb{1}$	118.8(4)	-154.0(3)	-35.2(7)	-5.5(1)	-5.6(1)	-0.26(1)	0.08(1)	0.27(1)
${}^{16}\text{O}$	1.0	NN	319(1)	-453(1)	-134(2)					
	1.0	$3N E\tau$	370(1)	-500(1)	-130(2)	-44(1)	-55(1)	0.85(1)	0	8.50(4)
	1.0	$3N E\mathbb{1}$	367(1)	-497(1)	-131(2)	-41(1)	-54(1)	0.72(1)	-4.03(5)	15.7(1)
	1.2	NN	377(1)	-528(2)	-151(3)					
	1.2	$3N E\tau$	556(4)	-712(3)	-156(7)	-202(3)	-101(2)	-0.72(9)	-94(2)	-5.43(3)
	1.2	$3N E\mathbb{1}$	377(1)	-529(1)	-152(2)	-26(1)	-34(1)	0.94(1)	4.53(8)	1.90(1)

coming from the $3N$ force in ${}^6\text{Li}$ and ${}^{16}\text{O}$ (Table X) clearly shows the issue. A large negative V_D contribution in ${}^{16}\text{O}$ for the soft $E\tau$ potential drives the system to a strongly bound state. In fact, even though the total energy at the two-body level is similar to that of the other soft potentials for $A = 16$, the individual expectation values for the kinetic energy and the two-body potential are severely larger, consistent with a very compact system. The $3N$ force adds then ≈ 13 MeV per nucleon, roughly half coming from the also increased TPE contribution, and half from V_D . In the case of the $R_0 = 1.0$ fm cutoff, instead, the $3N$ force in both parametrizations adds only < 3 MeV per nucleon to the total two-body energy, with similar TPE contributions and a balance between $\langle V_D \rangle$ and $\langle V_E \rangle$. This is still true in ${}^6\text{Li}$ also for $R_0 = 1.2$ fm, but the balance is broken for the soft $E\tau$ potential in ${}^{16}\text{O}$. The main reason for such behavior can be attributed to the large value of c_D for this potential (see Table IV), particularly effective for $A > 6$. Note that the energies given by the sum $E_{\text{kin}} + v_{ij} + v_{ijk}$ of Table X do not correspond to the constrained evolution results reported in Tables VIII and IX. This is a consequence of the mixed estimates necessary to evaluate the expectation value of the individual components of the Hamiltonian. Because the Hamiltonian commutes with itself, its expectation value is not extrapolated. Therefore, the total energy does not necessarily correspond to the sum of its extrapolated pieces, unless the trial wave function is the true ground-state wave function (see Ref. [1] for details).

As has been discussed briefly above and in more detail in Refs. [23,47], locally regulated chiral interactions spoil the Fierz rearrangement freedom used to select one of the six possible operators that are consistent with the symmetries of the theory for the contact interaction at N^2 LO, V_E . This means that results at finite cutoff depend on this choice. However, these additional regulator artifacts are absorbed by higher-order LECs in chiral EFT [47]. Furthermore, the dependence is typically within the truncation uncertainties (an exception occurs for denser or heavier systems such as neutron matter beyond saturation density, or as shown above, ${}^{16}\text{O}$). In these cases, since the next order in chiral EFT where $3N$ contacts appear is next-to-next-to-next-to-next-to-leading

order, a significant challenge at this point, one can use instead the parametrization V_{EP} of the contact interaction introduced in Ref. [23], which projects onto the total spin $S = 1/2$ and total isospin $T = 1/2$ triples. These are the triples that survive in the infinite (momentum-space) cutoff limit, and thus this parametrization partially restores the Fierz rearrangement freedom. However, the V_{EP} parametrization involves spin/isospin operators beyond quadratic order and presents a challenge to the direct inclusion in the AFDMC propagation. We leave the exploration of this parametrization to future works.

F. Charge form factors and Coulomb sum rules

One- and two-body point-nucleon densities are calculated as

$$\rho_N(r) = \frac{1}{4\pi r^2} \langle \Psi | \sum_i \mathcal{P}_{N_i} \delta(r - |\mathbf{r}_i - \mathbf{R}_{\text{cm}}|) | \Psi \rangle, \quad (69)$$

$$\rho_{NN}(r) = \frac{1}{4\pi r^2} \langle \Psi | \sum_{i < j} \mathcal{P}_{N_i} \mathcal{P}_{N_j} \delta(r - |\mathbf{r}_i - \mathbf{r}_j|) | \Psi \rangle, \quad (70)$$

where \mathcal{P}_{N_i} is the projector operator of Eq. (68). With the current definitions, ρ_N and ρ_{NN} integrate to the number of nucleons and the number of nucleon pairs, respectively.

As opposed to the charge radius, densities are not observables themselves, but the one-body densities can be related to physical quantities experimentally accessible via electron-nucleon scattering processes, such as the longitudinal elastic (charge) form factor. In fact, the charge form factor can be expressed as the ground-state expectation value of the one-body charge operator [56], which, ignoring small spin-orbit contributions in the one-body current, results in the following expression:

$$F_L(q) = \frac{1}{Z} \frac{G_E^p(Q_{\text{el}}^2) \tilde{\rho}_p(q) + G_E^n(Q_{\text{el}}^2) \tilde{\rho}_n(q)}{\sqrt{1 + Q_{\text{el}}^2/(4m_N^2)}}, \quad (71)$$

where $\tilde{\rho}_N(q)$ is the Fourier transform of the one-body point-nucleon density defined in Eq. (69), and $Q_{\text{el}}^2 = \mathbf{q}^2 - \omega_{\text{el}}^2$ is the four-momentum squared, with $\omega_{\text{el}} = \sqrt{q^2 + m_A^2} - m_A$ the

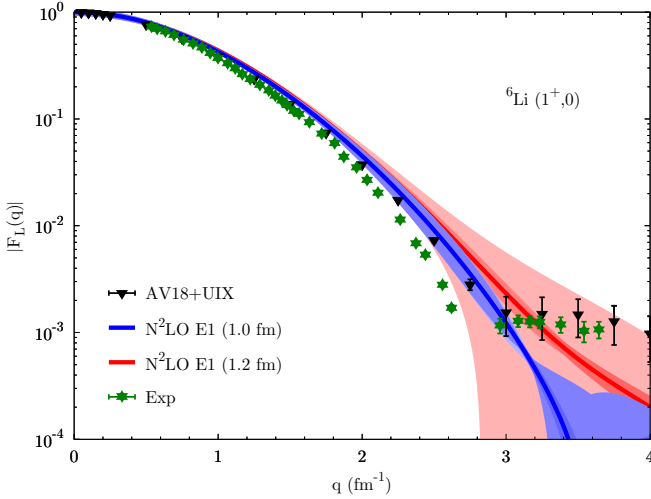


FIG. 7. Charge form factor in ${}^6\text{Li}$. The solid blue (red) line is the AFDMC result for the $\text{N}^2\text{LO } E1$ potential with cutoff $R_0 = 1.0(1.2)$ fm. Lighter shaded areas indicate the uncertainties from the truncation of the chiral expansion. Darker shaded areas are the theoretical error bands only taking into account NLO and N^2LO results. Black triangles are the VMC one-body results for AV18+UIX [58]. The experimental data are taken from Ref. [59].

energy transfer corresponding to the elastic peak, m_A being the mass of the target nucleus. $G_E^N(Q^2)$ are the nucleon electric form factors, for which we adopt Kelly's parametrization [57].

The charge form factors of ${}^6\text{Li}$, ${}^{12}\text{C}$, and ${}^{16}\text{O}$ are shown in Figs. 7–9, respectively. In all the plots, the blue (red) curve is the AFDMC result for the $\text{N}^2\text{LO } E1$ potential ($E\tau$ for ${}^{12}\text{C}$), with cutoff $R_0 = 1.0(1.2)$ fm. Monte Carlo error bars are typically of the size of the lines within the momentum range considered here. Lighter shaded areas indicate the uncertainties from the truncation of the chiral expansion,

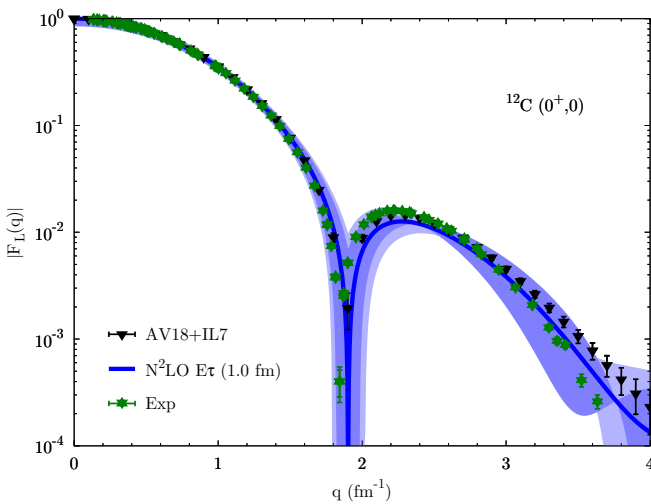


FIG. 8. Charge form factor in ${}^{12}\text{C}$. In blue are the AFDMC results for the $E\tau$ parametrization of the $3N$ force and cutoff $R_0 = 1.0$ fm. Black triangles are the GFMC one-body results for AV18+IL7 [60]. The experimental data are taken from Ref. [61]. Updated from Ref. [33].

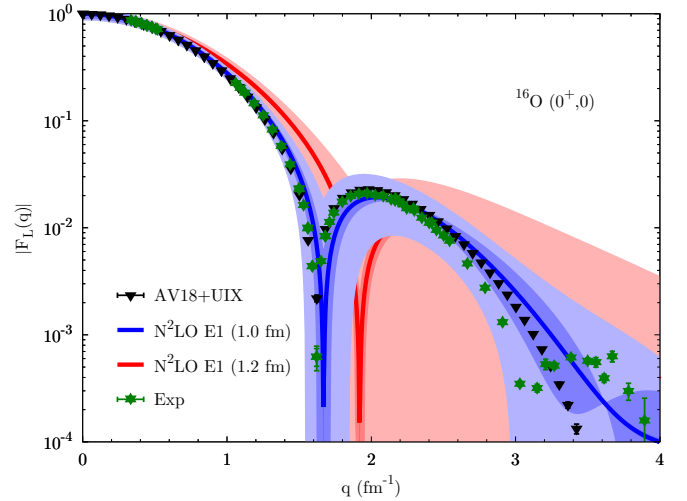


FIG. 9. Charge form factor in ${}^{16}\text{O}$. In blue (red) are the AFDMC results as in Fig. 7. Black triangles are the cluster-VMC one-body results for AV18+UIX [62]. Experimental data are from Sick, based on Refs. [55,63,64].

according to Eq. (65). Darker shaded areas are instead the theoretical error bands only considering the last term of the prescription, i.e., taking into account the NLO and N^2LO results only. AFDMC results are compared to experimental data and to available Monte Carlo calculations employing the phenomenological potentials and one-body charge operators only. No two-body operators are included in the calculation of the charge form factors in the current work. However, as shown in Refs. [58,60,65] for the three different systems, such operators give a measurable contribution only for $q > 2 \text{ fm}^{-1}$, as they basically include relativistic corrections.

The charge form factor of ${}^6\text{Li}$ for the $E1$ interaction is compatible with experimental data at low momentum for both cutoffs, with larger theoretical uncertainties for the soft potential. Results for the $E\tau$ parametrization show a similar behavior. The discrepancy for $q \gtrsim 2 \text{ fm}^{-1}$ is due to the missing two-body currents. In fact, AFDMC results for local chiral forces are compatible with the VMC one-body results for AV18+UIX [58] up to high momentum.

A similar physical picture is given for both ${}^{12}\text{C}$ and ${}^{16}\text{O}$, for which the positions of the first diffraction peaks in the form factors are well reproduced by the hard potentials within the theoretical error bands, and deviations from the experimental data occur at high momentum only. For the soft $E1$ interaction, instead, the description of the charge form factor in ${}^{16}\text{O}$ is less accurate, with the position of the first diffraction peak overestimated, and the slope of $F_L(q)$ for $q = 0$ underestimated, consistent with the smaller charge radius compared to the experimental value. The difference with respect to the experimental results is, however, not as dramatic as for the soft $E\tau$ potential (see Ref. [33]), and it is mostly covered by the very large theoretical error bands. These, in particular, are dominated by the LO contributions to the theoretical error estimate, as shown by the difference between lighter and darker bands in the form factor.

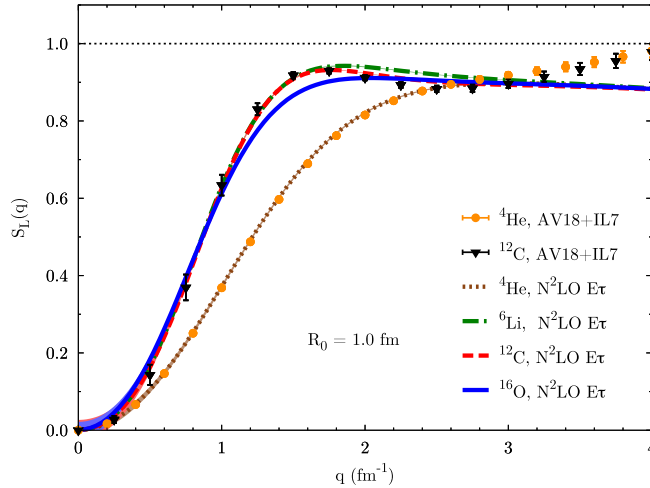


FIG. 10. Coulomb sum rule for $4 \leq A \leq 16$. Lines refer to AFDMC results for the $N^2LO E\tau$ potential with cutoff $R_0 = 1.0$ fm. Solid symbols are the GFMC one- plus two-body results for AV18+IL7 [60,62]. Shaded areas indicate the statistical Monte Carlo uncertainty.

Finally, it is interesting to note that, for all three systems, the local chiral interactions with the hard cutoff $R_0 = 1.0$ fm give the same physical description of the charge form factor as the phenomenological potentials, provided that one-body charge operators only are included in the calculation.

Two-body densities are related to the Coulomb sum rule, which is defined as the energy integral of the electromagnetic longitudinal response function. As with the charge form factor, the Coulomb sum rule can be written as a ground-state expectation value [56], leading to the relation

$$\begin{aligned}
 S_L(q) = & \frac{1}{Z} \frac{1}{G_E^{p2}(Q_{qe}^2)} \frac{1}{1 + Q_{qe}^2/(4m_N^2)} \\
 & \times \{ G_E^{p2}(Q_{qe}^2) [\tilde{\rho}_{pp}(q) + Z] \\
 & + G_E^{n2}(Q_{qe}^2) [\tilde{\rho}_{nn}(q) + (A - Z)] \\
 & + 2 G_E^p(Q_{qe}^2) G_E^n(Q_{qe}^2) \tilde{\rho}_{np}(q) \\
 & - [G_E^p(Q_{qe}^2) \tilde{\rho}_p(q) + G_E^n(Q_{qe}^2) \tilde{\rho}_n(q)]^2 \}, \quad (72)
 \end{aligned}$$

where $\tilde{\rho}_{NN}(q)$ is the Fourier transform of the two-body point-nucleon densities defined in Eq. (70), and $Q_{qe}^2 = \mathbf{q}^2 - \omega_{qe}^2$, with ω_{qe} the energy transfer corresponding to the quasielastic peak. Although the Coulomb sum rule is not directly an experimental observable (experimental information can be extracted, however, from the longitudinal response function, as done in Ref. [66] for ^{12}C), it is still an interesting quantity for the study of integral properties of the response of a nuclear many-body system to an external probe.

We report in Fig. 10 the Coulomb sum rule for $4 \leq A \leq 16$ using the $N^2LO E\tau$ potential with cutoff $R_0 = 1.0$ fm. The GFMC results for 4He and ^{12}C [60,62] employing the AV18+IL7 potential are also shown for comparison. The discrepancy between the AFDMC and GFMC results above $\approx 3 \text{ fm}^{-1}$ is due to the missing two-body currents in the

present calculation. For lower momenta the description of the sum rule is remarkably consistent with that provided by phenomenological potentials. Moreover, the results for ^{12}C are compatible with the available experimental data as extracted in Ref. [66], as shown already in Ref. [33]. All p -shell nuclei show a similar profile for $S_L(q)$, with a peak around 1.6 fm^{-1} , slightly more pronounced for open-shell systems ($A = 6, 12$). The same observations hold for the $E\parallel$ parametrization of the $3N$ force and for both cutoffs, with the Coulomb sum rule results of 4He and 6Li being very close to those shown in Fig. 10. An exception is the case of ^{16}O , for which $S_L(q)$ is largely different for the $E\tau$ parametrization and the softer cutoff, as already shown in Ref. [33].

VII. SUMMARY

We presented a detailed description of the AFDMC method for nuclei, with particular attention given to the construction of the trial wave function, the propagation of $3N$ forces, and the constrained/unconstrained imaginary-time evolution. We reported a series of test results for these technical aspects of the algorithm.

We performed AFDMC calculations of nuclei with $3 \leq A \leq 16$ using local chiral EFT interactions up to N^2LO , completing and expanding the results of Ref. [33]. Both two- and three-body potentials were considered, the latter described by two different operator structures, namely $E\tau$ and $E\parallel$. Two coordinate-space cutoffs, $R_0 = 1.0$ and $R_0 = 1.2$ fm, were used, with results presented at each order of the chiral expansion and for each $3N$ parametrization. To this aim, a new fit of the three-body LECs c_D and c_E was presented for the $E\parallel$ parametrization with the soft cutoff $R_0 = 1.2$ fm.

Binding energies and charge radii were shown for all the systems, and results for the charge form factor in 6Li , ^{12}C , and ^{16}O were also reported. For all these observables, the AFDMC results were supported by statistical Monte Carlo errors and theoretical errors coming from the truncation of the chiral expansion. Finally, the Coulomb sum rule for systems with $4 \leq A \leq 16$ was also shown.

The outcomes of this work confirm that local chiral interactions fit to few-body observables give a very good description of the ground-state properties of nuclei up to ^{16}O . This is true for both harder and softer interactions, even though the latter imply larger theoretical uncertainties coming from LO contributions to the truncation error estimate. We found that the overbinding in ^{16}O for the soft $E\tau$ parametrization of the $3N$ force is generated by large attractive contributions from the large value of the LEC c_D . Therefore, it will be very interesting to explore further $3N$ fits and operator choices in heavier nuclei as well as dense matter.

ACKNOWLEDGMENTS

We thank I. Tews, A. Lovato, A. Roggero, and R. F. Garcia Ruiz for many valuable discussions. The work of D.L. was supported by the U.S. Department of Energy, Office of Science, Office of Nuclear Physics, under Contract No. DE-SC0013617, and by the NUCLEI SciDAC program. The work of S.G. and J.C. was supported by the NUCLEI SciDAC program, by the

U.S. Department of Energy, Office of Science, Office of Nuclear Physics, under Contract No. DE-AC52-06NA25396, and by the LDRD program at LANL. The work of J.E.L. and A.S. was supported by the ERC Grant No. 307986 STRONGINT and the BMBF under Contract No. 05P15RDFN1. K.E.S. and C.P. were supported by the National Science Foundation Grant No. PHY-1404405. C.P. was also supported by a Wally Stoelzel Fellowship from the Department of Physics at Arizona State University. Computational resources have been provided by Los Alamos Open Supercomputing via the Institutional Computing (IC) program, and by the National Energy Research Scientific Computing Center (NERSC), which is supported by the U.S. Department of Energy, Office of Science, under Contract No. DE-AC02-05CH11231, by the Lichtenberg high performance computer of the TU Darmstadt, and by the Extreme Science and Engineering Discovery Environment (XSEDE), which is supported by the National Science Foundation Grant No. ACI-1548562.

APPENDIX: CALCULATING TWO-BODY CORRELATIONS

Given $R = \{\mathbf{r}_1, \dots, \mathbf{r}_A\}$ the particle coordinates, $S = \{s_1, \dots, s_A\}$ the spin/isospin configurations, and $|\chi_\gamma\rangle$ the $|p \uparrow\rangle$, $|p \downarrow\rangle$, $|n \uparrow\rangle$, $|n \downarrow\rangle$ basis

$$\begin{aligned} |\chi_1\rangle &= |(1,0,0,0)\rangle, \\ |\chi_2\rangle &= |(0,1,0,0)\rangle, \\ |\chi_3\rangle &= |(0,0,1,0)\rangle, \\ |\chi_4\rangle &= |(0,0,0,1)\rangle. \end{aligned} \quad (\text{A1})$$

We define the Slater matrix element

$$S_{\alpha i} = \langle \alpha | \mathbf{r}_i | s_i \rangle = \sum_{\gamma=1}^4 \langle \alpha | \mathbf{r}_i | \chi_\gamma \rangle \langle \chi_\gamma | s_i \rangle, \quad (\text{A2})$$

where $|\alpha\rangle$ contains the radial orbitals and spherical harmonics of Eq. (59). When acting with two-body correlations on the mean-field part of the wave function, the Slater matrix is updated by each of the correlation operators. These updates are computed using the identity

$$\det(S^{-1} S') = \frac{\det S'}{\det S}, \quad (\text{A3})$$

where S' is the matrix that has been updated by the action of a single operator. To reduce the number of operations, the ratio of determinants for a pair of operators, $\mathcal{O}_{ij} = \mathcal{O}_i \mathcal{O}_j$, is written in the form

$$\frac{\langle \Phi | \mathcal{O}_{ij} | RS \rangle}{\langle \Phi | RS \rangle} = \sum_{\gamma=1}^4 \sum_{\delta=1}^4 d_{2b}(\chi_\gamma, \chi_\delta, ij) \langle \chi_\gamma \chi_\delta | \mathcal{O}_{ij} | s_i s_j \rangle, \quad (\text{A4})$$

with

$$\begin{aligned} d_{2b}(\chi_\gamma, \chi_\delta, ij) &= \frac{\langle \Phi | R, s_1, \dots, s_{i-1}, \chi_\gamma, s_{i+1}, \dots, s_{j-1}, \chi_\delta, s_{j+1}, \dots, s_A \rangle}{\langle \Phi | RS \rangle}, \end{aligned} \quad (\text{A5})$$

where χ_γ and χ_δ replace s_i and s_j , respectively. The d_{2b} matrix elements are derived from the precalculated matrix elements $P_{\chi,ij}$:

$$d_{2b}(\chi_\gamma, \chi_\delta, ij) = \det \begin{pmatrix} P_{\chi_\gamma,ii} & P_{\chi_\gamma,ij} \\ P_{\chi_\delta,ji} & P_{\chi_\delta,jj} \end{pmatrix}, \quad (\text{A6})$$

where

$$\begin{aligned} P_{\chi_\gamma,ij} &= \sum_{\alpha} S_{j\alpha}^{-1} S_{\alpha i} (s_i \leftarrow \chi_\gamma), \\ P_{\chi_\delta,ij} &= \sum_{\alpha} S'_{j\alpha}^{-1} S'_{\alpha i} (s_j \leftarrow \chi_\delta). \end{aligned} \quad (\text{A7})$$

Though the above relations only address two-body operators, this method can be generalized to arbitrary N -body operators as well. To include additional operators the matrix elements $P_{\chi,ij}$ need to be updated:

$$P_{\chi_\eta,mn} = \sum_{\alpha} S''_{n\alpha}^{-1} S''_{\alpha m} (s_m \leftarrow \chi_\eta), \quad (\text{A8})$$

where

$$S''_{\alpha m}(s_m) = \begin{cases} S_{\alpha m}, & m \neq i, \\ \langle \alpha | \mathcal{O}_i | \mathbf{r}_i | s_i \rangle, & m = i. \end{cases} \quad (\text{A9})$$

To calculate the updated inverse matrix, the identity of Eq. (A3) is used with $S' \leftarrow S''$. Both sides of the identity are expanded, and like terms are grouped, noting that when $j \neq i$, $S''_{mi} = S'_{mi}$.

The wave function with linear correlations [Eq. (55)] is calculated by first acting on the coordinate and spin/isospin configurations with each possible operator, and calculating the sum of each term $\sum_{\chi_\gamma, \chi_\delta} d_{2b}(\chi_\gamma, \chi_\delta, ij) \langle \chi_\gamma, \chi_\delta | f_{ij}^p \mathcal{O}_{ij}^p | s_i s_j \rangle$. The expectation value of the potential on the linear wave function is calculated including correlation and potential operators, \mathcal{O}_{ij}^c and \mathcal{O}_{ij}^p respectively, organized in the form $(\mathbb{1} + \mathcal{O}_{ij}^c) \mathcal{O}_{kl}^p$, which includes four potentially distinct operators. For this calculation the P matrix is updated twice, once for \mathcal{O}_i^c and once for \mathcal{O}_j^c , where $\mathcal{O}_{ij}^c = \mathcal{O}_i^c \mathcal{O}_j^c$ as before. The ratio of determinants is calculated following Eq. (A4), using the updated distribution d_{2b}'' .

The quadratic wave function includes the same correlation terms of the linear wave function plus a piece with two additional operators, resulting in structures like $\mathbb{1} + \mathcal{O}_{ij}^c + \mathcal{O}_{ij}^c \mathcal{O}_{kl}^c$. The operators up to linear terms are treated as above. The quadratic product of operators is handled in the same fashion as the expectation value of the potential acting on the linear wave function, i.e., the P matrix is updated twice, once for \mathcal{O}_i^c and once for \mathcal{O}_j^c , and the ratio of determinants is calculated with the updated distributions. It follows that the calculation of the correlation operators for the quadratic wave function requires $O(A^4)$ operations, compared to $O(A^2)$ for the linear wave function.

The expectation value of the potential acting on the quadratic wave function requires the product of six operators $\mathcal{O}_{ij}^c \mathcal{O}_{kl}^c \mathcal{O}_{mn}^p$. As a result, a total of four updates are needed to calculate the quadratically correlated terms for the potential. After including the updated distributions for the \mathcal{O}_{ij}^c operators, the same distributions are updated two more times for the \mathcal{O}_{kl}^c terms. These quadratically updated distributions are then used to calculate the expectation value of the potential as

before. It follows that the calculation of the expectation value of the potential acting on the quadratic wave function requires $O(A^6)$ operations, compared to $O(A^4)$ for the linear wave function.

The two-body correlations of Eq. (55) have the same operator structure as the AV6' potential. The Cartesian breakup of

such structure generates 39 \mathcal{O}_{ij}^c operators: 9 $\sigma_{\alpha i} \sigma_{\beta j}$, 3 $\tau_{\gamma i} \tau_{\gamma j}$, and 27 $\sigma_{\alpha i} \sigma_{\beta j} \tau_{\gamma i} \tau_{\gamma j}$ operators. The number of operators can be reduced to 15 if, instead of Cartesian coordinates, one uses the pair distance \mathbf{r}_{ij} and two orthogonal coordinates. This reduces the number of operators used in the spatially dependent part of the tensor term, $3 \boldsymbol{\sigma}_i \cdot \hat{\mathbf{r}}_{ij} \boldsymbol{\sigma}_j \cdot \hat{\mathbf{r}}_{ij}$, from 9 to 3.

-
- [1] J. Carlson, S. Gandolfi, F. Pederiva, S. C. Pieper, R. Schiavilla, K. E. Schmidt, and R. B. Wiringa, *Rev. Mod. Phys.* **87**, 1067 (2015).
- [2] S. Gandolfi, J. Carlson, and S. C. Pieper, *Phys. Rev. Lett.* **106**, 012501 (2011).
- [3] S. Gandolfi, J. Carlson, and S. Reddy, *Phys. Rev. C* **85**, 032801 (2012).
- [4] P. Maris, J. P. Vary, S. Gandolfi, J. Carlson, and S. C. Pieper, *Phys. Rev. C* **87**, 054318 (2013).
- [5] S. Gandolfi, A. Lovato, J. Carlson, and K. E. Schmidt, *Phys. Rev. C* **90**, 061306 (2014).
- [6] S. Gandolfi, J. Carlson, S. Reddy, A. W. Steiner, and R. B. Wiringa, *Eur. Phys. J. A* **50**, 10 (2014).
- [7] M. Buraczynski and A. Gezerlis, *Phys. Rev. Lett.* **116**, 152501 (2016).
- [8] M. Buraczynski and A. Gezerlis, *Phys. Rev. C* **95**, 044309 (2017).
- [9] A. Sarsa, S. Fantoni, K. E. Schmidt, and F. Pederiva, *Phys. Rev. C* **68**, 024308 (2003).
- [10] P. B. Demorest, T. Pennucci, S. M. Ransom, M. S. E. Roberts, and J. W. T. Hessels, *Nature (London)* **467**, 1081 (2010).
- [11] J. Antoniadis, P. C. C. Freire, N. Wex, T. M. Tauris, R. S. Lynch, M. H. van Kerkwijk, M. Kramer, C. Bassa, V. S. Dhillon, T. Driebe, J. W. T. Hessels, V. M. Kaspi, V. I. Kondratiev, N. Langer, T. R. Marsh, M. A. McLaughlin, T. T. Pennucci, S. M. Ransom, I. H. Stairs, J. van Leeuwen, J. P. W. Verbiest, and D. G. Whelan, *Science* **340**, 1233232 (2013).
- [12] E. Epelbaum, H.-W. Hammer, and U.-G. Meißner, *Rev. Mod. Phys.* **81**, 1773 (2009).
- [13] R. Machleidt and D. R. Entem, *Phys. Rep.* **503**, 1 (2011).
- [14] E. Epelbaum, H. Krebs, and U.-G. Meißner, *Phys. Rev. Lett.* **115**, 122301 (2015).
- [15] A. Ekström, G. R. Jansen, K. A. Wendt, G. Hagen, T. Papenbrock, B. D. Carlsson, C. Forssén, M. Hjorth-Jensen, P. Navrátil, and W. Nazarewicz, *Phys. Rev. C* **91**, 051301 (2015).
- [16] B. D. Carlsson, A. Ekström, C. Forssén, D. F. Strömberg, G. R. Jansen, O. Lilja, M. Lindby, B. A. Mattsson, and K. A. Wendt, *Phys. Rev. X* **6**, 011019 (2016).
- [17] D. R. Entem, R. Machleidt, and Y. Nosyk, *Phys. Rev. C* **96**, 024004 (2017).
- [18] P. Reinert, H. Krebs, and E. Epelbaum, [arXiv:1711.08821](https://arxiv.org/abs/1711.08821).
- [19] A. Ekström, G. Hagen, T. D. Morris, T. Papenbrock, and P. D. Schwartz, *Phys. Rev. C* **97**, 024332 (2018).
- [20] A. Gezerlis, I. Tews, E. Epelbaum, S. Gandolfi, K. Hebeler, A. Nogga, and A. Schwenk, *Phys. Rev. Lett.* **111**, 032501 (2013).
- [21] A. Gezerlis, I. Tews, E. Epelbaum, M. Freunek, S. Gandolfi, K. Hebeler, A. Nogga, and A. Schwenk, *Phys. Rev. C* **90**, 054323 (2014).
- [22] I. Tews, S. Gandolfi, A. Gezerlis, and A. Schwenk, *Phys. Rev. C* **93**, 024305 (2016).
- [23] J. E. Lynn, I. Tews, J. Carlson, S. Gandolfi, A. Gezerlis, K. E. Schmidt, and A. Schwenk, *Phys. Rev. Lett.* **116**, 062501 (2016).
- [24] M. Piarulli, L. Girlanda, R. Schiavilla, R. N. Pérez, J. E. Amaro, and E. R. Arriola, *Phys. Rev. C* **91**, 024003 (2015).
- [25] M. Piarulli, L. Girlanda, R. Schiavilla, A. Kievsky, A. Lovato, L. E. Marcucci, S. C. Pieper, M. Viviani, and R. B. Wiringa, *Phys. Rev. C* **94**, 054007 (2016).
- [26] M. Piarulli, A. Baroni, L. Girlanda, A. Kievsky, A. Lovato, E. Lusk, L. E. Marcucci, S. C. Pieper, R. Schiavilla, M. Viviani, and R. B. Wiringa, *Phys. Rev. Lett.* **120**, 052503 (2018).
- [27] J. E. Lynn, J. Carlson, E. Epelbaum, S. Gandolfi, A. Gezerlis, and A. Schwenk, *Phys. Rev. Lett.* **113**, 192501 (2014).
- [28] J. E. Lynn, I. Tews, J. Carlson, S. Gandolfi, A. Gezerlis, K. E. Schmidt, and A. Schwenk, *Phys. Rev. C* **96**, 054007 (2017).
- [29] J.-W. Chen, W. Detmold, J. E. Lynn, and A. Schwenk, *Phys. Rev. Lett.* **119**, 262502 (2017).
- [30] P. Klos, J. E. Lynn, I. Tews, S. Gandolfi, A. Gezerlis, H.-W. Hammer, M. Hoferichter, and A. Schwenk, *Phys. Rev. C* **94**, 054005 (2016).
- [31] P. W. Zhao and S. Gandolfi, *Phys. Rev. C* **94**, 041302 (2016).
- [32] S. Gandolfi, H.-W. Hammer, P. Klos, J. E. Lynn, and A. Schwenk, *Phys. Rev. Lett.* **118**, 232501 (2017).
- [33] D. Lonardoni, J. Carlson, S. Gandolfi, J. E. Lynn, K. E. Schmidt, A. Schwenk, and X. B. Wang, *Phys. Rev. Lett.* **120**, 122502 (2018).
- [34] R. B. Wiringa and S. C. Pieper, *Phys. Rev. Lett.* **89**, 182501 (2002).
- [35] J. Hoppe, C. Drischler, R. J. Furnstahl, K. Hebeler, and A. Schwenk, *Phys. Rev. C* **96**, 054002 (2017).
- [36] N. Metropolis, A. W. Rosenbluth, M. N. Rosenbluth, A. H. Teller, and E. Teller, *J. Chem. Phys.* **21**, 1087 (1953).
- [37] D. M. Ceperley, *Rev. Mod. Phys.* **67**, 279 (1995).
- [38] H. F. Trotter, *Proc. Am. Math. Soc.* **10**, 54 (1959).
- [39] S. C. Pieper, Monte carlo calculations of nuclei, in *Microscopic Quantum Many-Body Theories and Their Applications, Proceedings of a European Summer School Held at Valencia, Spain, 8–19 September 1997*, edited by J. Navarro and A. Polls (Springer, Berlin, 1998), pp. 337–357.
- [40] B. S. Pudliner, V. R. Pandharipande, J. Carlson, S. C. Pieper, and R. B. Wiringa, *Phys. Rev. C* **56**, 1720 (1997).
- [41] W. M. C. Foulkes, L. Mitas, R. J. Needs, and G. Rajagopal, *Rev. Mod. Phys.* **73**, 33 (2001).
- [42] M. Pervin, S. C. Pieper, and R. B. Wiringa, *Phys. Rev. C* **76**, 064319 (2007).
- [43] S. Zhang and H. Krakauer, *Phys. Rev. Lett.* **90**, 136401 (2003).
- [44] S. Zhang, J. Carlson, and J. E. Gubernatis, *Phys. Rev. B* **55**, 7464 (1997).
- [45] G. Ortiz, D. M. Ceperley, and R. M. Martin, *Phys. Rev. Lett.* **71**, 2777 (1993).
- [46] G. M. Hale, D. C. Dodder, and K. Witte (unpublished).

- [47] L. Huth, I. Tews, J. E. Lynn, and A. Schwenk, *Phys. Rev. C* **96**, 054003 (2017).
- [48] E. Epelbaum, H. Krebs, and U.-G. Meißner, *Eur. Phys. J. A* **51**, 53 (2015).
- [49] J. Beringer, J. F. Arguin, R. M. Barnett, K. Copic, O. Dahl, D. E. Groom, C. J. Lin, J. Lys, H. Murayama, C. G. Wohl, W. M. Yao, P. A. Zyla, C. Amsler, M. Antonelli, D. M. Asner *et al.* (Particle Data Group), *Phys. Rev. D* **86**, 010001 (2012).
- [50] J. L. Friar, J. Martorell, and D. W. L. Sprung, *Phys. Rev. A* **56**, 4579 (1997).
- [51] A. Ong, J. C. Berengut, and V. V. Flambaum, *Phys. Rev. C* **82**, 014320 (2010).
- [52] P. Mueller, I. A. Sulai, A. C. C. Villari, J. A. Alcántara-Núñez, R. Alves-Condé, K. Bailey, G. W. F. Drake, M. Dubois, C. Eléon, G. Gaubert, R. J. Holt, R. V. F. Janssens, N. Levesne, Z.-T. Lu, T. P. O'Connor, M.-G. Saint-Laurent, J.-C. Thomas, and L.-B. Wang, *Phys. Rev. Lett.* **99**, 252501 (2007).
- [53] W. Nörtershäuser, T. Neff, R. Sánchez, and I. Sick, *Phys. Rev. C* **84**, 024307 (2011).
- [54] I. Sick, *Phys. Lett. B* **116**, 212 (1982).
- [55] I. Sick and J. S. McCarthy, *Nucl. Phys.* **A150**, 631 (1970).
- [56] K. W. McVoy and L. Van Hove, *Phys. Rev.* **125**, 1034 (1962).
- [57] J. J. Kelly, *Phys. Rev. C* **70**, 068202 (2004).
- [58] R. B. Wiringa and R. Schiavilla, *Phys. Rev. Lett.* **81**, 4317 (1998).
- [59] G. C. Li, I. Sick, R. R. Whitney, and M. R. Yearian, *Nucl. Phys. A* **162**, 583 (1971).
- [60] A. Lovato, S. Gandolfi, R. Butler, J. Carlson, E. Lusk, S. C. Pieper, and R. Schiavilla, *Phys. Rev. Lett.* **111**, 092501 (2013).
- [61] H. De Vries, C. W. De Jager, and C. De Vries, *At. Data Nucl. Data Tables* **36**, 495 (1987).
- [62] D. Lonardoni, A. Lovato, S. C. Pieper, and R. B. Wiringa, *Phys. Rev. C* **96**, 024326 (2017).
- [63] W. Schütz, *Z. Phys. A* **273**, 69 (1975).
- [64] I. Sick (unpublished).
- [65] B. Mihaila and J. H. Heisenberg, *Phys. Rev. Lett.* **84**, 1403 (2000).
- [66] A. Lovato, S. Gandolfi, J. Carlson, S. C. Pieper, and R. Schiavilla, *Phys. Rev. Lett.* **117**, 082501 (2016).